ARTICLE

Crystal Facet and Architecture Engineering of Metal Oxide Nanonetwork Anodes for High-Performance Potassium Ion Batteries and Hybrid Capacitors

Chao-Hung Chang,[†] Kuan-Ting Chen,[†] Yi-Yen Hsieh, Che-Bin Chang, and Hsing-Yu Tuan*

Read Online

ACCESS | Metrics & More | Article Recommendations | Supporting Information

ABSTRACT: Metal oxides are considered as prospective dual-functional anode candidates for potassium ion batteries (PIBs) and hybrid capacitors (PIHCs) because of their abundance and high theoretic gravimetric capacity; however, due to the inherent insulating property of wide band gaps and deficient ion-transport kinetics, metal oxide anodes exhibit poor K^+ electrochemical performance. In this work, we report crystal facet and architecture engineering of metal oxides to achieve significantly enhanced K^+ storage performance. A bismuth antimonate ($BiSbO_4$) nanonetwork with an architecture of perpendicularly crossed single crystal nanorods of majorly exposed (001) planes are synthesized *via* CTAB-mediated growth. (001) is found to be the preferential surface diffusion path for superior adsorption and K^+ transport, and in addition, the interconnected nanorods gives rise to a robust matrix to enhance electrical conductivity and ion transport, as well as buffering dramatic volume change during insertion/extraction of K^+. Thanks to the synergistic effect of facet and structural engineering of $BiSbO_4$ electrodes, a stable dual conversion-alloying mechanism based on reversible six-electron transfer per formula unit of ternary metal oxides is realized, proceeding by reversible coexistence of potassium peroxide conversion reactions ($KO_2 \leftrightarrow K_2O$) and Bi_xSb_y alloying reactions ($BiSb \leftrightarrow KBiSb \leftrightarrow K_3BiSb$). As a result, $BiSbO_4$ nanonetwork anodes show outstanding potassium ion storage in terms of capacity, cycling life, and rate capability. Finally, the implementation of a $BiSbO_4$ nanonetwork anode in the *state-of-the-art* full cell configuration of both PIBs and PIHCs shows satisfactory performance in a Ragone plot that sheds light on their practical applications for a wide range of K^+-based energy storage devices. We believe this study will propose a promising avenue to design advanced hierarchical nanostructures of ternary or binary conversion-type materials for PIBs, PIHCs, or even for extensive energy storage.
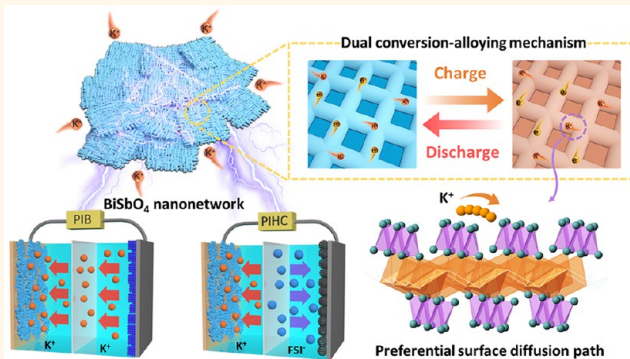
KEYWORDS: bismuth antimonate, bimetallic oxides, potassium ion storage, anodes, batteries, capacitors

Because of the rapid development of portable electronic devices, electric vehicles, and large-scale grid integration equipment, the demand is constantly growing for lithium-ion (Li^+) energy storage devices (*e.g.*, lithium-ion batteries (LIBs) and lithium-ion hybrid capacitors (LIHCs)).[1,2] However, the major concern for the further availability and scale-up of Li^+ storage devices is the uneven distribution of Li resources and the limited global reserves for the depletion of Li raw materials.[3,4] Potassium (K) has electrochemical properties similar to Li, abundant reserves, and relatively low cost, making K^+ energy storage an attractive Li^+ alternative.[5−7] The low standard redox potential of K^+/K (−2.93 V *vs* −3.04 V for Li^+/Li) enables relatively high battery

voltages to operate electrode materials at a suitable voltage platform. Compared with sodium ion (Na^+), the weaker Lewis acidity of K^+ achieves high ion conductivity due to its low solvation energy in the electrolyte.[8−10] However, due to the large ion radius of K^+ (1.38 Å *vs* 0.76 Å of Li^+), the electrode

Scheme 1. BiSbO₄ Nanonetwork Electrode and Its Working Mechanism for K⁺ Storage and Applications on PIBs and PIHCs[a]
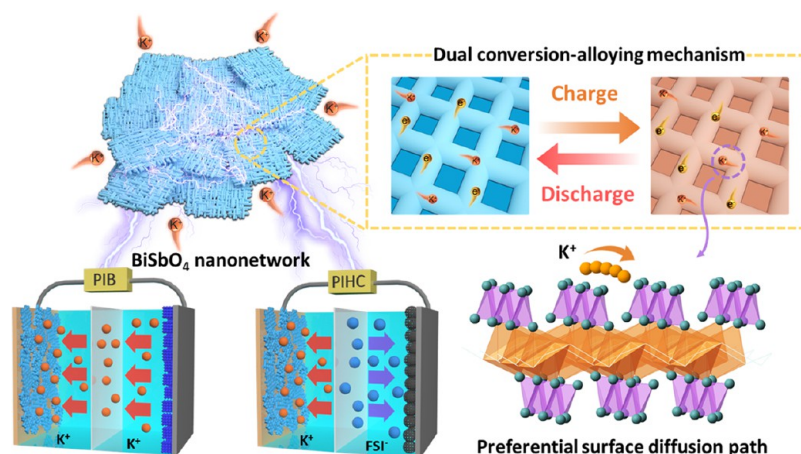
[a]BiSbO₄ nanonetwork composed of interconnected nanorod architecture enhances electric conductivity, ion transport, as well as buffering dramatic volume change during K⁺ insertion/extraction *via* preferential surface diffusion paths for superior adsorption and transport of K⁺ to proceed a stable dual conversion-alloying mechanism of ternary metal oxides. The implementation of the BiSbO₄ nanonetwork in full cell configuration of PIBs and PIHCs is demonstrated.

structure is irreversibly deteriorated upon repeated insertion/extraction of ions. The slow Faraday reaction and the fast capacitive reaction results in imbalance kinetics, irreversibility, and short lifespan for potassium ion batteries (PIBs) and hybrid capacitors (PIHCs). Therefore, carbonaceous materials, a widely used anode for Li⁺ energy storage devices, suffer from the disadvantages described above and present a relatively low theoretical capacity less than 300 mA h g⁻¹ (*e.g.*, KC_8: 279 mA h g⁻¹).[11−13] Recently, conversion/alloying-based materials (*e.g.*, metal oxide, and metal chalcogenides) have been regarded as promising anode candidates for PIBs and PIHCs.[14−17] In the cycling process, the electrode undergoes a series of various physical (*e.g.*, diffusion, adsorption of ion, and structural surface tension) and chemical changes (*e.g.*, alloying, conversion reactions, and side effects in electrolyte) which needs the optimization and engineering of the structure and composition of electrodes to achieve reversible K⁺ chemical reactions.[18,19]

Metal oxide materials are earth-abundant, environmentally friendly, and easy to fabricate on a large scale.[20,21] When used as a storage device anode, the conversion/alloying reaction transfers more electrons than other materials, so it is expected to obtain a higher specific capacity/capacitance than carbon-based materials.[22] However, metal oxides are generally considered as wide band gap semiconductors or even insulators. Therefore, poor ion transport kinetics and electric conductivity lead to low ion diffusion coefficients and high resistance, causing severe capacity decay.[23] During the conversion/alloying reactions between metal oxides and K⁺, a dramatic volume change (∼400%) occurs, resulting in pulverization of the electrode film. To overcome these drawbacks, the most widely used strategy is to reduce the size and incorporate them with carbon coating/composites.[24] Although a nanoscale material shortens the diffusion ion transport path inside the electrode matrix, the increase in grain boundaries inevitably results in solid electrode resistance. Several integration approaches of carbonaceous materials, such as coating carbon shells, carbon nanotube, and graphene, were introduced to improve electrical conductivity of metal oxides for rapid charge transfer and enhanced structural stability.[25−29] However, metal oxide/carbon composite electrodes often contain up to 20−50% carbon content,

which are carbonized at high temperatures above 500 °C, and thus, their structural morphologies are mainly determined by the carbon scaffold.

Engineering the crystal surface and structure of metal oxides may improve K⁺ storage performance. For instance, the surface energy highly depends on the crystal orientation, where the exposed surface can promote the interfacial effects of favorable adsorption and diffusion pathways to improve ion diffusion, adsorption, and deposition.[30] Dathar *et al.* compared the surface energies of various pathways of Li⁺ jumping into $FePO_4$ structure.[31] Density functional theory (DFT) simulations show that the entrance of the channel can be regarded as a rate-determining step in electrochemical dynamics that determines the most possible jumps in surface diffusion. Furthermore, certain high surface energy interfaces may attract more Li⁺, thereby increasing the reversible capacity or reducing the activation energy of diffusion pathways. For example, Pan *et al.* found that the diffusion of lithium ions to the SnO_2 (211) surface is much easier than to other surfaces and that the high surface energy of the highly exposed (211) surface can attract more Li⁺ to accelerate the oxidation reduction reaction kinetics, thus increasing the specific capacitance as electrodes for hybrid type capacitor.[32] It is worth noting that if the architecture is designed to be interconnected together, it will be useful to enhance the structural stability and ensure the efficiency of electron transport, which have been demonstrated in several assembled metal oxide nanonetworks such as nanowire clusters and honeycomb structure.[33,34] However, the in-depth concept of preferential diffusion pathway of ions and electron transfer has rarely discussed in the K⁺ storage system.

Herein, we report a metal oxide electrode, BiSbO₄ nanonetwork, which is an architecture composed of perpendicularly crossed single crystal that achieves enhanced K⁺ storage. Scheme 1 depicts the K⁺ storage mechanism of the BiSbO₄ nanonetwork and their uses as anodes on PIBs and PIHCs. The BiSbO₄ nanonetwork electrode has the following advantageous characteristics: (1) network composed of tightly connected rods reduce particle aggregation, pose higher mechanical strength, and provide multichannel electronic/ionic pathways. The interconnected structure well aligned in the certain
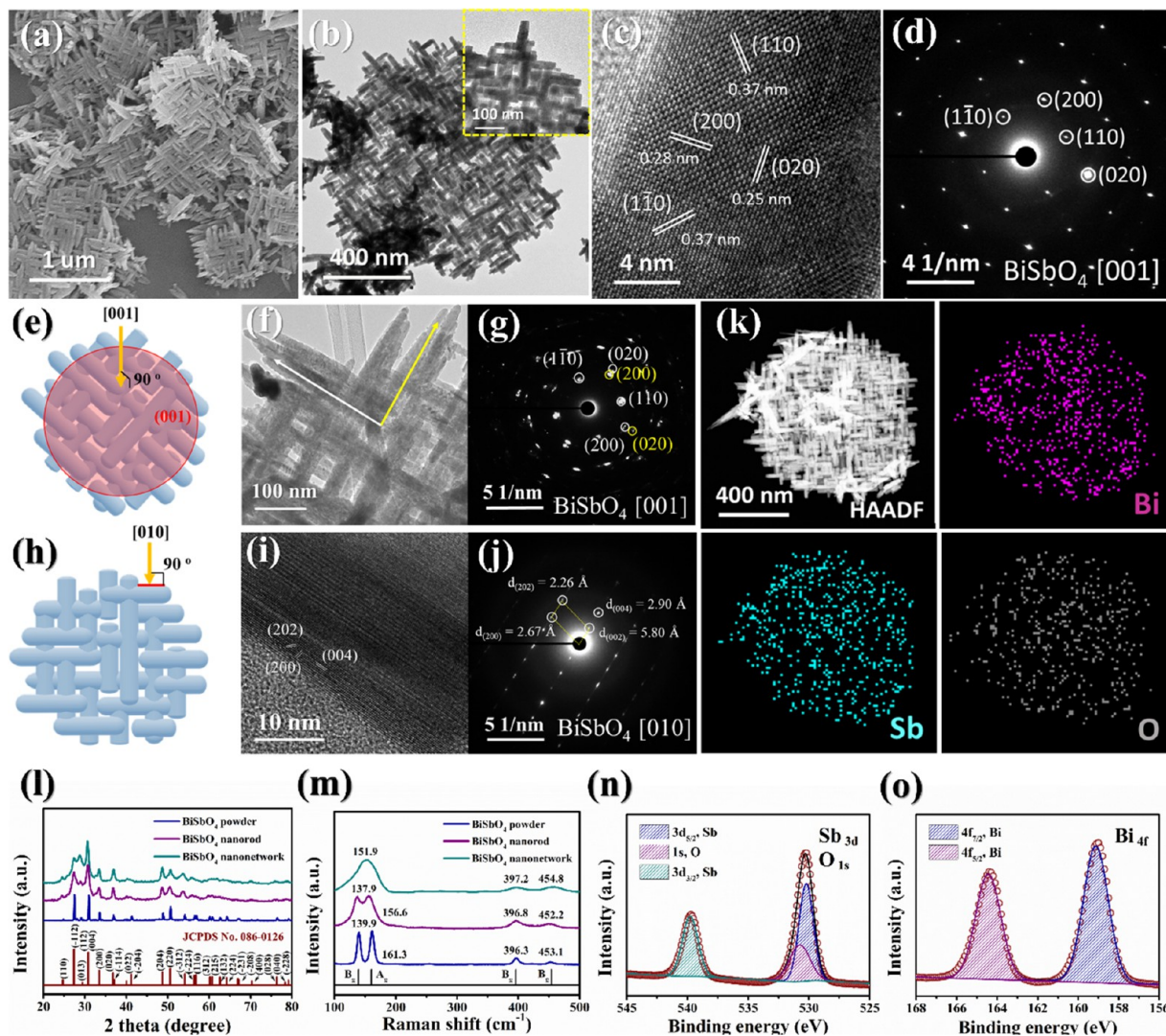
Figure 1. (a) Morphology characterization in SEM images of BiSbO$_4$ samples in a hydrothermal method with addition of 75 mg of CTAB. (b) High-magnification TEM images of the BiSbO$_4$ network. The insets present the low-magnification TEM image of the BiSbO$_4$ network. The HRTEM analysis, SAED pattern, and scheme of (c,d) single nanorod on BiSbO$_4$ network, (e−g) (001)-orientated plane, (h−j) (010)-orientated plane, and (k) EDS elements mapping of a BiSbO$_4$ network. Material characterization of (l) XRD patterns, and (m) Raman spectra of BiSbO$_4$ powders, BiSbO$_4$ nanorods, and BiSbO$_4$ networks. High-resolution XPS spectrum in (n) Sb 3d and O 1s and (o) Bi 4f region.

directions enhances the surface diffusion at the interface with the electrolyte. The void space between each rod is capable to withstand volume expansion/contraction stress. (2) Experimental results of electrochemical impedance spectroscopy (EIS) and galvanostatic intermittent titration (GITT) combined with theoretical density functional theory (DFT) reveal that the exposed (001) plane falls on the lowest energy barrier for K$^+$ along the aligned diffusion tunnel. This preferential diffusion path enables enhanced adsorption and migration of K$^+$ as well as highly efficient charge transfer. (3) The surface and structure regulation can further facilitate the dual reversible conversion-alloying reactions of BiSbO$_4$ electrodes with K$^+$. The initial formation of potassium oxide (K$_2$O) can reduce the volume expansion that occurs between the Bi and Sb atomic layers, thereby allowing the Bi$_x$Sb$_y$ alloying reactions (BiSb ↔ KBiSb ↔ K$_3$BiSb). Moreover, the simultaneous conversion reaction of potassium peroxide (KO$_2$ ↔ K$_2$O) also contributes a considerable amount of capacity. Therefore, among the currently reported metal oxide anodes, BiSbO$_4$ exhibits the most balanced K$^+$ storage properties. Finally, we fabricated a PIB

full battery coupled with Prussian blue nanoparticle (PBNPs) cathodes and a PIHC full cell with activated carbon (AC) cathodes to evaluate the feasibility of the BiSbO$_4$ network anodes in the *state-of-the-art* storage systems.

RESULTS AND DISCUSSION

BiSbO$_4$ of various morphologies were prepared by reacting Bi(NO$_3$)$_3$·5H2O with Sb$_2$O$_3$ in the presence of cetyltrimethylammonium bromide (CTAB) *via* a hydrothermal approach at 180 °C. A network of metal oxide materials can be synthesized *via* a CTAB-mediated crystal growth where CTAB is easily ionized to form CTA$^+$ cations with hydrophobic alkyl chains as a cationic surfactant.[35] Because of the difference in surface energy, it tends to be adsorbed on the specific surface of the nucleated nanoparticle, resulting in an anisotropic network growth.[36] As shown in Figure S1a, without the addition of CTAB (CTAB-0), spindle-like BiSbO$_4$ nanorods were formed. The amount of CTAB greatly influences the final product morphology. In Figure S1b, with the addition of 25 mg of CTAB (CTAB-25), a nanonetwork composed of spindle-like rods was obtained due to
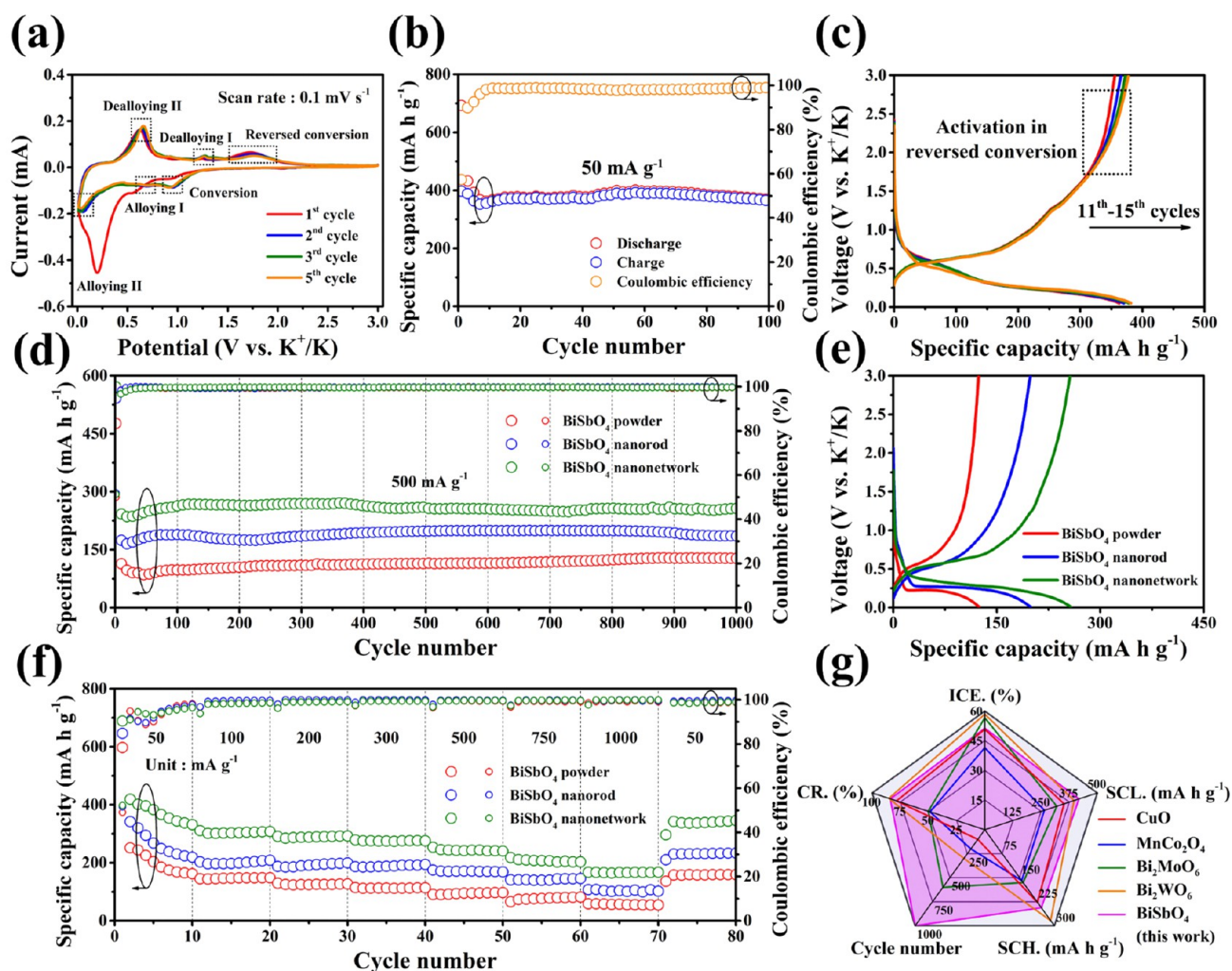
Figure 2. Electrochemical performances of $BiSbO_4$ PIBs in half cells. (a) CV profiles at a scan rate of 0.1 mV s^{-1}. (b) Cycling performance at a current density of 50 mA g^{-1}. (c) GCD curves correspond to (b) from the 11th to the 15th cycle. (d) Long-term cycling performance at a current density of 500 mA g^{-1}. (e) GCD curves in the 800th cycle correspond to (d). (f) Rate performance at various current densities from 50 to 1000 mA g^{-1}. (g) Comparison results of initial Coulombic efficiency (ICE), specific capacity at low and high rates (SCL and SCH), long-term cycle number, and capacity retention (CR) with other previously reported anode materials of metal oxide.

the relatively low capping ability of CTA$^+$. When the amount of CTAB was increased to 50 mg (CTAB-50), the spindle-shaped rods transformed into nanorods with a smoother surface aligned in specific directions (Figure S1c). Figures 1a and S1d reveal the morphology outline of $BiSbO_4$ networks synthesized in the presence of 75 mg of CTAB (CTAB-75). The formed network structure is established by a plane with a length and a width close to 1 μm and composed of straight nanorods with a length and a width of approximately 200 and 50 nm, respectively. In addition, when the amount of CTAB increases to 100 and 125 mg, the growth of the (013) plane begins to compete with the growth of the (004) plane (Figure S2). Transmission electron microscope (TEM) images in Figures 1b and its inset show that the interwoven meshwork is well established with interspersed voids. In addition, the high-resolution TEM (HRTEM) image shows the crystal lattice details and atomic arrangement (Figure 1c), where the nanorod grows along the [200] direction, and the fringe spacing is 0.28, 0.25, and 0.37 nm, which can be indexed to (200), (020), and (110), respectively. The selected area electron diffraction (SAED) pattern of a single nanorod (Figure 1d) can be indexed to a zone axis of [001], revealing an exposed facet of (001). The SAED pattern of $BiSbO_4$ displays a spot pattern

(single crystal) instead of a ring pattern (randomly arrangement, polycrystalline). To present more clearly exposed facet of (001) in $BiSbO_4$ network, the schematic diagram in Figure 1e indicates the different zone axes, illustrating that the exposed network surface vertical to the zone axis of [001] belongs to the (001) plane (red region). The TEM image and SAED pattern of $BiSbO_4$ network in Figure 1f,g can also prove that the zone axis is [001], which is perpendicular to (001) plane, and clearly exhibited two growth directions (white and yellow arrow), which is an architecture composed of perpendicularly crossed single crystal. According to Bragg's law, if we want to further observe the d-spacing of the (001) plane, we must take an HRTEM image from the side view of the $BiSbO_4$ network, as shown in the Figure 1h. Therefore, the side-viewed HRTEM analysis (Figure 1i) and SAED pattern (Figure 1j) demonstrate the d-spacing and lattice spot of the (001) plane when the zone axis is [010], respectively. The elemental composition measured by energy-dispersive X-ray spectroscopy (EDS) (Figure 1k) indicates that the as-prepared $BiSbO_4$ network is uniformly composed of Bi, Sb, and O elements, and the detailed distribution ratio is presented in Table S1.

The X-ray diffraction (XRD) technique, Raman spectrum, and X-ray photoelectron spectroscopy (XPS) were used to confirm the purity, vibrational models, and elemental characteristics to further investigate the structural properties and chemical state of the $BiSbO_4$. All of the diffraction peaks in the selected 2-θ angle range are illustrated in Figure 1l, and the crystal phase is labeled as $BiSbO_4$ (JCPDS no. 86-0126). The $BiSbO_4$ powder was sintered at high temperature from the precursor of metal oxides (Figure S3). Given that the factor groups of $BiSbO_4$ have been computed on Raman-active modes in previous literature, Figure 1m shows the corresponding phonons of A_g and B_g types at the zone center.[37] The phonon doublet peaks at frequencies near 140 and 161 cm^{-1} are partially overlapped, which may be attributed to the difference in crystallinity. As shown in Figure S4, a full survey of the spectrum revealed the presence of Bi, Sb, O, and C, which can be attributed to the environmental conditions. In the Bi 4f spectrum, the characteristic peaks at 159.2 and 164.5 eV can be clearly distinguished as Bi−O bonding by 4f core splitting into Bi $4f_{7/2}$ and Bi $4f_{5/2}$ (Figure 1o). Specifically, the composition of the three distinct peaks in the spectra of Sb 3d and O 1s were located at 530.2, 531.4, and 539.8 eV, respectively. The peaks at 530.2 and 539.8 eV can be considered as the formation of the Sb−O bond, which is consistent with the O 1s peak at 531.4 eV (Figure 1n). A slight chemical shift of the binding energy with a single metal oxide phase is proposed due to the variation of the oxidation states in $BiSbO_4$.[38] In Figure S5, several distinct peaks were observed in the spectrum of C 1s, 284.8, 286.1, and 288.1 eV, which are consistent with the Sp^3 hybrid carbon and the C−O bonds derived from the ligand with surfactants. According to the relative sensitivity factor (RSF), from high-resolution spectra, the content of each element content is calculated and listed in Table S2. To further identify that there is no carbon content in this work, an NCSH element analysis instrument is used and shown in Table S3.

The K$^+$ storage behaviors of $BiSbO_4$ were evaluated by a series of measurements using metallic potassium as the counter electrode in a coin-type CR2032 half cell. The cyclic voltammetry (CV) curves of the $BiSbO_4$ nanonetwork at a scan rate of 0.1 mV s^{-1} are illustrated in Figure 2a, and the CV curves of $BiSbO_4$ powders and rods are presented in Figure S6, indicating that the discharge/charge curves have similar characteristics. During the initial discharge, three cathodic peaks can be observed. The first approximately 0.9 V can be interpreted as the formation of the solid electrolyte interface (SEI) layer by the decomposition of electrolyte. In the following cycle, other cathodic peaks near 0.6 and 0.2 V disappear, which can be ascribed to the irreversible conversion and alloying process of $BiSbO_4$. In the reversed process, the three anodic peaks located in the interval between 0.6 and 1.8 V are related to the dealloying process of K(Bi, Sb) and K_3(Bi, Sb) and the formation of KO_2, where the continuous redox peaks overlap in the subsequent CV curves that reveal the high reversibility and stability of $BiSbO_4$ networks. Figures 2b and S7 show a galvanostatic charge−discharge (GCD) test and voltage profile of $BiSbO_4$ networks at a current density of 50 mA g^{-1}, exhibiting initial discharge and charge capacities of 692.7 and 397.4 mA h g^{-1}, respectively, corresponding to the initial Coulombic efficiency of 57.4%. The initial capacity loss can be mainly associated with the irreversible conversion process of $BiSbO_4$ and the reduction of electrolyte during the growth of the SEI layer. Owing to the activation of $BiSbO_4$, the repeated insertion of K$^+$ provides a large number of electrode active sites, and the

capacity gradually increases. After 100 cycles, the electrode still remained a reversible capacity of 368.5 mA h g^{-1}. Moreover, the GCD curves (Figure 2c) recorded at a current density of 50 mA g^{-1} reveal that the slight increase in capacity at the plateau is consistent with the reverse conversion process in the CV measurement. This activation may be attributed to the process of conversion into KO_2. The comparison of the long-term cycling performance and corresponding Coulombic efficiency of $BiSbO_4$ powder, $BiSbO_4$ nanorods, and $BiSbO_4$ nanonetwork electrodes is displayed in Figure 2d. At the current density of 500 mA g^{-1}, three samples can maintain extremely high stability under repeated insertion and extraction of K$^+$, and all of the capacities loss per cycle are not over 0.05%. In particular, the $BiSbO_4$ nanonetwork exhibited a reversible capacity of 256.5 mA h g^{-1} after 1000 cycles, whereas the $BiSbO_4$ powder and $BiSbO_4$ nanorod can only deliver lower capacities of 127.4 and 185.1 mA h g^{-1}, respectively. As shown in Figure 2e, by comparing the corresponding charge/discharge curves of the three samples after 800 cycles, details regarding the difference in capacity contribution can be clarified. The reason for the lowest capacity of $BiSbO_4$ powder may be due to the large particle size of its structure, which restricts K$^+$ diffusion from the surface to the interior part. The short plateau at lower potential (0.5 and 0.25 V) and almost perpendicular voltage profile at higher potential indicate that the conversion and alloy reactions are not complete. However, both the $BiSbO_4$ nanorod and $BiSbO_4$ network show a slight increase in capacity at high potentials, whereas the $BiSbO_4$ network can obtain an extended platform at low potential. Therefore, the specific capacity and cycle stability of the network structure are much better than the other morphology, which is more suitable for K$^+$ storage. Figure 2f shows the rate performance of $BiSbO_4$ of various morphologies at different current densities. Among them, the $BiSbO_4$ nanonetwork exhibited superior cycling responses of 331.5, 307.8, 292.5, 275.9, 240.2, 203.1, and 167.1 mA h g^{-1} at current densities of 50, 100, 200, 300, 500, 750, and 1000 mA g^{-1}. In contrast, $BiSbO_4$ powder delivered the lowest rate capabilities under the same conditions, which are 162.4, 148.2, 125.4, 113.7, 96.8, 79.6, and 54.7 mA h g^{-1}, respectively. When the current density was returned to 50 mA g^{-1}, the $BiSbO_4$ nanonetwork also showed higher reversible K$^+$ storage than the $BiSbO_4$ powder and the $BiSbO_4$ nanorod. It is worth noting that all three samples have a capacity decay phenomenon at a current density of 50 mA g^{-1}, which also occurred in other literature on metal oxides for K$^+$ storage.[39] We suspect that in the early stage of cycling the slow kinetics can make the material transform as fully as possible, in which its composition would gradually change from $BiSbO_4$ to (Bi, Sb) and K_2O via a dual conversion/alloying reaction. However, because of its intrinsic poor electronic conductivity, it can be inferred from Figure 2b,c that the activation of the reversed conversion reaction gradually improved and stabilized after about 10 cycles. After the early stage, the capacities of the three samples were all returned to a stable state at a current density of 1000 mA g^{-1} (Figure S8). Therefore, we believe that benefiting from more active sites helps to increase the K$^+$ capacity in the network structure and better migration conditions. The interconnected structure can provide a continuous transition path for electrons and ion diffusion, enabling efficient charge carriers in electrochemical reactions and being beneficial toward reducing the polarization caused by current changes. In the radar chart of Figure 2g, the comparison of various metal oxide anodes without assistance of carbonaceous materials in five aspects, including initial
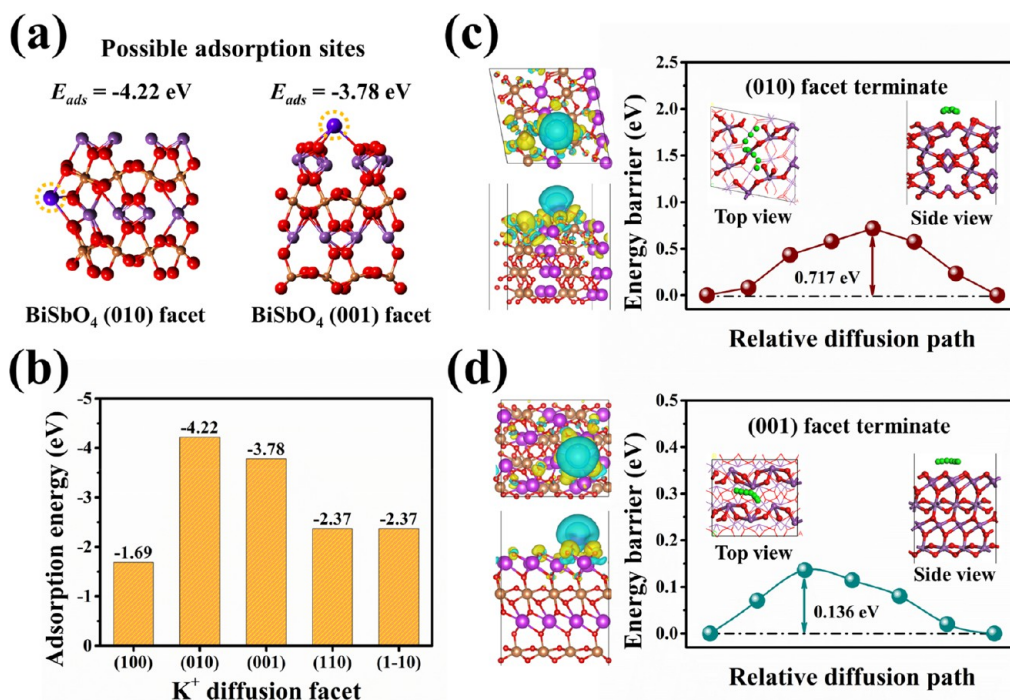
Figure 3. Theoretical calculation of K+ adsorption and diffusion on BiSbO4 facets. (a) Structural models of possible adsorption sites with K+ adsorption energy on the (010) and (001) planes. (b) Other adsorption energies according to the exposed facets of BiSbO4 network. Energy barrier and diffusion path in top view and side of (c) (010) and (d) (001) facets with differential charge density analysis. The yellow and blue isosurfaces are represented as electron accumulation and depletion, respectively.

Coulombic efficiency (ICE), low rate specific capacity at 50 mA g^{-1} (SCL), high rate specific capacity at 500 mA g^{-1} (SCH), and cyclability such as cycle number and capacity retention rate (CR), are shown.[40−43] Owing to the inevitable capacity loss inherent from the conversion mechanism, the irreversible reaction involved in the first cycle requires that the ICE of all metal oxides is less than 60%. The BiSbO4 networks not only deliver high gravimetric capacity at both low and high current densities but also accomplish a cycle stability of up to 1000 cycles due to intercommunicated diffusion tunnels and the robust framework of oxygen layer in BiSbO4 nanonetwork.

To ascertain the detailed reason for the performance improvement, conclusions can be drawn from the electrochemical impedance spectroscopy (EIS) test performed in the range of 20 mHz to 100 kHz in Figure S9a. Apparently, after 100 cycles, the high-frequency semicircle of BiSbO4 network presents the smallest diameter in the Nyquist plot, implying that the lowest total resistance associated with charge transfer (R_{ct}) and formed SEI layer (R_{sf}) in an analog equivalent circuit. Notably, the cycle dominated Warburg coefficient (σ) can be determined by incorporating with Fick's first law to obtain the Butler−Volmer equation in the components of impedance (Z) and frequency (ω), which is equivalent to the slope derived from the linear plot of $-\mathrm{Im}(Z)$ *vs* $\omega^{-1/2}$. Therefore, the diffusion coefficient of K+ can be further calculated according to the following formula in the prevalence of diffusion and low frequency range

$$D_{K^+} = \frac{0.5R^2T^2}{A^2n^4F^4C^2\sigma^2}$$

where R, T, and F are the ideal gas constant, thermodynamic temperature, and Faraday constant, respectively, while other algebras are the reaction condition of the electrodes. Among

them, A denotes the electrode area and n represents the number of transferred electrons, where the bulk concentration is symbolized as C. As shown in Figure S9b,c, the difference between the original state and the cyclic state of each electrode further verifies that the migration of K+ should be regulated by the different affinities to the facets, and the diffusion coefficient of K+ in the BiSbO4 network has been improved in the magnitude of $10^{-15}-10^{-14}$ cm^2 s^{-1}. To gain further insight into the contribution of the diffusion-controlled process and surface-controlled process to the K+ storage kinetics and mechanism, we analyzed the redox peak current of the CV curves at various scan rates (Figure S9d). On the basis of the CV measurement, the relationship between the peak current (i) and the scan rate (v) follows the equation

$$i = av^b$$

where a and b are constants in the power law. In particular, the b value as the fitted slope of $\log(i)$ vs. $\log(v)$ qualitatively shows the storage kinetics of the electrodes.[44] For the diffusion-controlled process, the peak current is proportional to the square root of the scan rate (b value of 0.5), which is dominated by the solid-state diffusion-limiting behavior. On the other side, the peak current is proportional to the scan rate in the surface-controlled process (b value of 1), indicating that the kinetic behavior is related to the electric double-layer capacitive response. As shown in Figure S9e, the b values of the anodic peak and cathodic peak are 0.751 and 0.798, respectively, which reflects that both the ion diffusion and the capacitive effect participate in the kinetics of K+ between BiSbO4 electrodes. Furthermore, the contribution ratio to the capacitance in the potential range of 0.01 to 3.0 V can be distinguished according to the equation
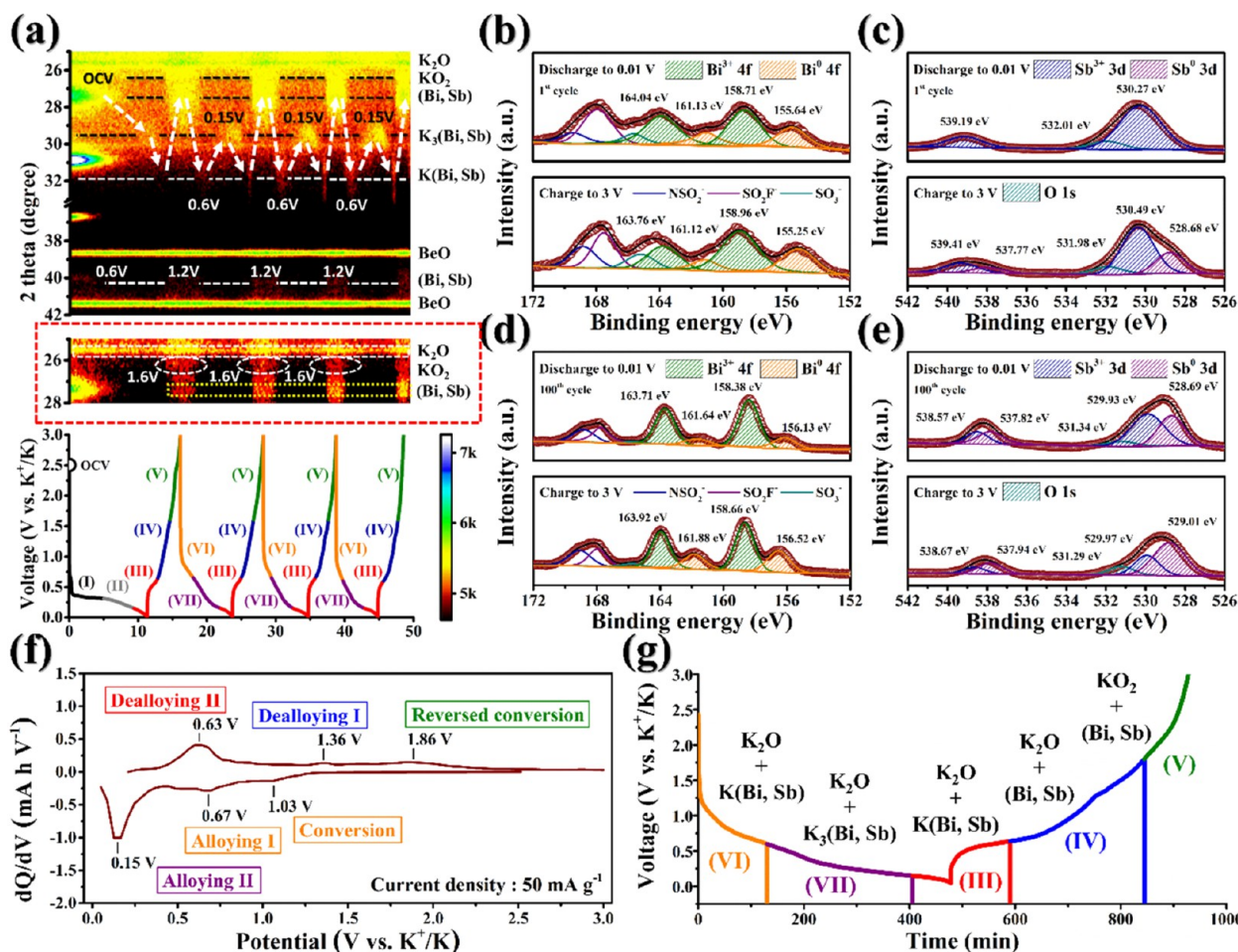
$$i = k_1v + k_2v^{1/2}$$

Figure 4. Analyses of K$^+$ storage mechanism in BiSbO$_4$. (a) Contour plot of the operando XRD pattern with magnified display ranged from 25° to 28°. (b−e) XPS spectra of Bi 4f and Sb 3d after discharging to 0.01 V and charging to 3 V at the 1st and 100th cycle. (f) Differential plot of GCD curve with identified reaction peaks. (g) Proposed reaction mechanism corresponding to GCD curve.

where k_1 and k_2 are the value of fitted slope and intercept in linear plot of v vs $v^{1/2}$ by proportion of both the contribution of surface control and the contribution of diffusion control (Figure S9f).[45] As shown in Figure S9g, as the scan rate increases from 0.1 to 0.9 mV s^{-1}, the percentage of capacitive contribution to BiSbO$_4$ electrodes increases from 27.69% of the total K$^+$ storage to 58.12%, suggesting that the increase in scan rates induces faster kinetics of the surface-dependent mechanism. Galvanostatic intermittent titration (GITT) measurements have been carried out to further provide the diffusion coefficient and migration barrier during discharge and charge process (Figure S9h). On the basis of GITT profiles, the diffusion ability of K$^+$ can be calculated quantitatively by mathematical derivation from Fick's second law

$$D_{K^+} = \frac{4}{\pi\tau}\left(\frac{n_m V_m}{S}\right)^2 \left(\frac{\Delta E_s}{\Delta E_t}\right)^2 \approx \frac{4}{\pi\tau} L^2 \left(\frac{\Delta E_s}{\Delta E_t}\right)^2 \left(\tau \ll \frac{L^2}{D_{K^+}}\right)$$

where n_m and V_m represent the molar number and molar volume of the electrode while S represents the electrode−electrolyte contact area.[46] Notably, the median fraction composed by these components can be simplified as the thickness of the overall electrode (L), which can be determined by cross-section SEM images in Figure S10. ΔE_s and ΔE_t are denoted as the equipoised voltage change induced by continuous current pulse and voltage change during the constant current pulse, while τ is the duration

of the current pulse. The derived diffusion coefficients of K$^+$ were presented as homologous values to the state of discharge and charge, ranging from 10^{-10} to 10^{-11} and 10^{-8} to 10^{-11} cm^2 s^{-1}, respectively (Figure S9i). Note that the inferior diffusion property in the discharge process can be regarded as the impediment from poor conductivity for charge transfer to convert into fully alloying phases. During the charge process, apparently, two sequential plateaus appear with different values of diffusion coefficient, indicating that the facile kinetics of two-step depotassiation reaction of Bi and Sb ensure a rapid movement of K$^+$.[47]

Moreover, we use the DFT calculation *via* the Vienna *Ab initio* Simulation Package (VASP) by way of the projector augmented wave (PAW) method to calculate localized interfacial behavior of BiSbO$_4$ with respect to K$^+$ storage. The configurations of (100), (010), and (001) and the symmetric layouts of (110) as well as (1−10) are discussed in detail (Figure S11). When K$^+$ is close to the material surface, it is noticeable that once the possible termination of a certain surface is determined, the adsorption site of K$^+$ can be calculated and the quantified value can be further simulated (Figure 3a). In view of the fact that the migration of K$^+$ between the neighboring stable poses a great influence on the surface charge transfer, it is also necessary to consider the energy barrier between the initial and final stable position. Figure 3b plots the adsorption energy of each facet of BiSbO$_4$, where the (010) facet possesses the lowest state (−4.22
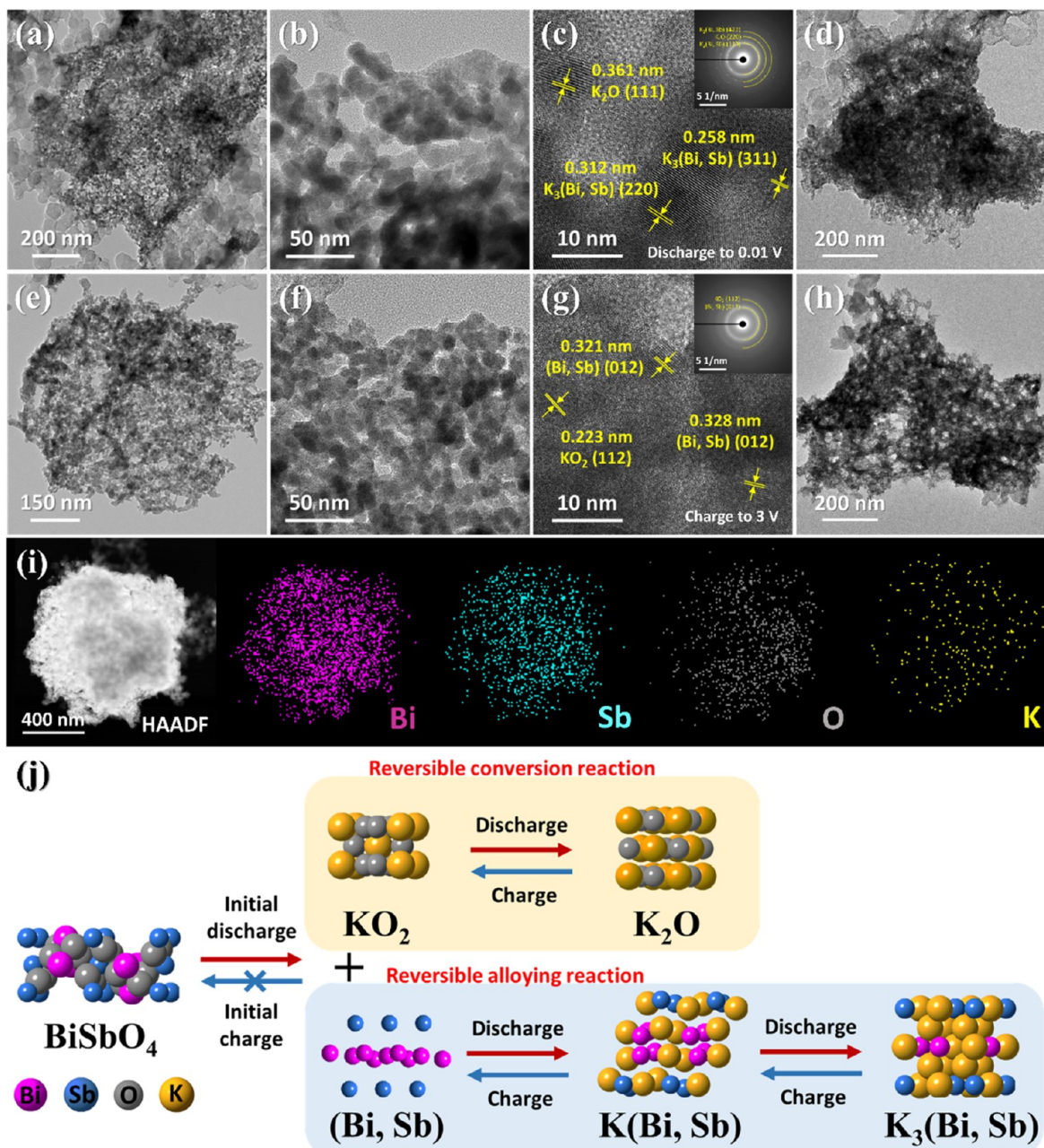
Figure 5. Post-mortem TEM observations of the cycled BiSbO₄ network anode. Morphology details and HRTEM images with corresponding SAED patterns of BiSbO₄: (a−d) discharged to 0.01 V and (e−h) charged to 3 V. (i) EDS elements mapping of BiSbO₄ network after cycling. (j) Schematic illustration of the K⁺ storage mechanism during the alloying and conversion process.

eV) to accommodate the K⁺ in the oxygen hollow position. However, regarding the diffusion path, the (010) facet must face the huge energy barrier of 0.717 eV caused by the attraction of surrounded oxygen atoms, whereas other facets of (100), (110), and (1−10) are also prone to be confined into the hollow site of oxygen (Figure S12). Notably, due to the open-tunnel structure, the vacancy spaces aligned in the [100] direction are well exposed on the (001) facet, which is proposed to promote K⁺ migration along the tunnel. Only the (001) facet exhibits a sufficiently comparable adsorption energy (−3.78 eV) with the (010) facet and the lowest energy barrier of BiSbO₄ is 0.136 eV, indicating a preferential reactive surface with K⁺ (Figure 3c,d). In addition, the deformation of the charge density revealing the dispersion of electrons in accumulation and depletion confirms the direction of electron transportation. Most of the charge in

BiSbO₄ is concentrated around O atoms, and the dissipated part is located in the sublayers of K atoms and Bi and Sb atoms on the (001) plane, indicating that the electron are easily transferred to the metal layer to form an electron transport route. Based on the theoretical results, it can be proposed that the crystal plane evolution of the BiSbO₄ network in the (001) facet significantly enhances the kinetic of the K⁺ storage process due to considerable interaction in the electrode/electrolyte interface.
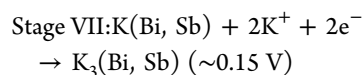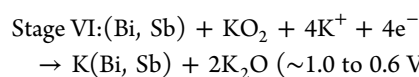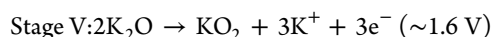
The storage mechanism of K⁺ in the BiSbO₄ nanonetwork was also investigated by *in situ* XRD measurement. Figure 4a depicts the *in situ* contour mapping in the selected 2-θ angle range to interpret the phase evolution of the BiSbO₄ electrode during the initial four cycles in different states. The peaks at 38.6° and 41.3° are from the oxidation of the beryllium window in the *in situ* test device, corresponding to BeO (JCPDS no. 35-0818). After

inserting K$^+$ into the electrode, the potential suddenly drops to around 0.4 V, beginning the conversion reaction of BiSbO$_4$ (stage I). The intensive diffraction peaks of 27.3°, 30.7°, and 36.8° are identified as (−112), (004), and (020) facets of BiSbO$_4$ (JCPDS no. 86-0126), which gradually disappeared and were accompanied by 25.5° and 40.5° pointing, respectively, to the (111) facet of K$_2$O (JCPDS no. 77-2176) and the (110) facet of (Bi, Sb) (JCPDS no. 07-9027). As the electrode discharged further, a peak of 29.7° was observed near 0.15 V (stage II), which is related to the fully alloying phase of K$_3$(Bi, Sb) (JCPDS no. 19-0935). It is worth mentioning that the weak crystallinity in the (220) facet of K$_3$(Bi, Sb) is related to the activation according to the continuous change of the voltage. As the reaction shifts to the charge process, the characteristic peak of K(Bi, Sb) (JCPDS no. 42-0791) appears at around 0.6 V (stage III) and is converted to (Bi, Sb) again at about 1.2 V (stage IV), indicating the multistep dealloying reaction from K$_3$(Bi, Sb) to (Bi, Sb). In the fully extracted state of K$^+$, no detected peaks can be attributed to the pristine BiSbO$_4$ phase. The peak of the K$_2$O phase always exists but the intensity becomes lower, and the KO$_2$ (JCPDS no. 39-0697) phase begins to appear, which shows the *in situ* (Bi, Sb) alloying formation and the reversible conversion of KO$_2$ around 1.6 V (stage V). The magnified display of the partial interval in the range of 25°−28° provides clearer evidence to confirm the repetitive characteristic peaks of KO$_2$ and the diffraction fringes of K$_2$O, KO$_2$, and (Bi, Sb), while the increasing intensity of (Bi, Sb) further elucidates the ongoing activation. Different from the first discharge process, on the contrary, the (Bi, Sb) alloying transforms into the intermediate of K(Bi, Sb) and thereafter continues to alloy with excessive K$^+$ with the emergence of K$_3$(Bi, Sb) (stages VI and VII). The subsequent charging process showed a process similar to that of the first cycle, thus revealing the reversible multistep insertion/extraction mechanism of K$^+$ based on both alloying and conversion reactions.[48] The composition of the unknown product during K$^+$ activation was further verified by XPS, and the circulating electrodes were in a different state after stabilization (Figure S13). As shown in Figure 4b,c, the characteristic peaks of SO$_3^-$, SO$_2$F$^-$, and NSO$_2^-$ functional groups can be seen, which can be designated as the interface composition derived from the electrolyte.[49] When the electrode is fully discharged, the doublet peaks of the Bi 4f spectrum at 155.6 and 161.1 eV are mainly related to the conversion to the K$_3$Bi phase, whereas the absence of the K$_3$Sb phase implied the stepwise activation in the first cycle. After returning to the fully charged state, the zero-valence peaks of Bi remained slightly deviated, while the deconvoluted peak of 528.7 eV of the Sb 3d spectrum is considered to be the decomposition of K−Sb−O bond. Therefore, the activation of BiSbO$_4$ can be used for the cleavage of the bond between the oxidation phase of the Bi−O and Sb−O bonds. Moreover, the further results of the cycled electrode are also illustrated in Figure 4d,e. In these two spectra, it is worth noting that the zero-valence distribution has a lower binding energy in the discharged state compared with the distribution in charged state, inferring the reversible reaction between the alloying phase and metallic phase.[50] According to the remaining obvious peaks of Bi^{3+} 4f and Sb^{3+} 3d core splitting, they come from the remaining compound composed of Bi−O and Sb−O bonding, which does not participate in the potassiation behavior. However, since the binding energy of the O 1s spectrum around 532 eV overlaps with the signal of the Sb 3d spectrum around 530 eV, the detail of oxidation states is still unclear. Figure 4f illustrates the

differential graph of the GCD curve marked with several distinguished redox peaks. The multistep reduction peaks show the conversion reaction of K$_2$O at around 1.0 V and two-step alloying transformation of (Bi, Sb) alloying around 0.6 and 0.15 V. The strong oxidation peak near 0.6 V is the first dealloying process from K$_3$(Bi, Sb) to K(Bi, Sb), while the one around 1.3 V is the second dealloying from K(Bi, Sb) to (Bi, Sb). The peak near 1.8 V indicates the reverse conversion from K$_2$O to KO$_2$ during the anodic process (Figure 4g).

The visual morphology and crystal structure during cycling of BiSbO$_4$ nanonetwork was investigated. As shown in Figure 5a,b, after discharge to 0.01 V, the TEM images reveal the well-interconnected shape of the BiSbO$_4$ network with a uniformly distributed SEI layer. The corresponding high-resolution TEM images and SAED patterns detail the information about the products formed by the reaction with K$^+$. The lattice fringes with a spacing of 0.361 and 0.312 nm can be designed as the (111) plane of K$_2$O and (110) plane of K$_3$(Bi, Sb), respectively (Figure 5c). At the fully charged state of 3.0 V, Figure 5e,f shows a further morphology of repeated K$^+$ migration, indicating that the stable framework can effectually accommodate to the mechanical stress derived from drastic volume change. From the high-resolution TEM image and SAED pattern displayed in Figure 5g, the lattice fringes with a spacing of 0.304 and 0.223 nm splitting into two reflection rings can be indexed as (Bi, Sb) alloying and (112) plane of KO$_2$, and it is concluded that the primary BiSbO$_4$ phase has irreversibly undergone conversion, resulting in reduced (Bi, Sb) alloying. As shown in Figure 5d,h, the structure is still maintained by the interwoven mesh structure after cycling. Furthermore, the HAADF image and EDS mapping results of the cycled BiSbO$_4$ network show that although the (Bi, Sb) alloy is formed, there is no obvious phase separation (Figure 5i). Therefore, with the combined operando XRD, XPS, and TEM analyses of the cycled electrodes, the reaction mechanism has been schematically illustrated in Figure 5j. The proposed reaction in conversion can be recognized and reasonable for balancing the chemical equation with the reversible existence of K$_2$O and KO$_2$ phases.

Stage I: BiSbO$_4$ + 8K$^+$ + 8e$^-$
→ (Bi, Sb) + 4K$_2$O (∼0.6 V)

Stage II: (Bi, Sb) + 3K$^+$ + 3e$^-$ → K$_3$(Bi, Sb) (∼0.15 V)

Stage III: K$_3$(Bi, Sb) → K(Bi, Sb) + 2K$^+$ + 2e$^-$ (∼0.6 V)

Stage IV: K(Bi, Sb) → (Bi, Sb) + K$^+$ + e$^-$ (∼1.2 V)

Stage V: 2K$_2$O → KO$_2$ + 3K$^+$ + 3e$^-$ (∼1.6 V)

Stage VI: (Bi, Sb) + KO$_2$ + 4K$^+$ + 4e$^-$
→ K(Bi, Sb) + 2K$_2$O (∼1.0 to 0.6 V)

Stage VII: K(Bi, Sb) + 2K$^+$ + 2e$^-$
→ K$_3$(Bi, Sb) (∼0.15 V)
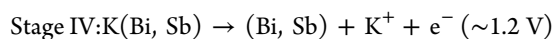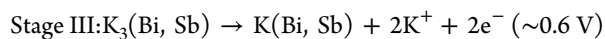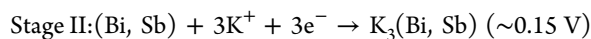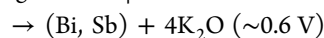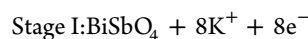
Inspired by the battery performance, diffusion kinetics, and the mechanism in these indices of electrochemical assessment in half cell devices, BiSbO$_4$ nanonetwork can be considered as a promising anode material to overcome the intrinsic drawback and provide a feasibility to further assemble with other cathode materials into a full battery in PIBs and PIHCs. In half cells, the infinite resource of K metal counter electrodes, also regarded as reference electrodes, highlights the performance of offsetting the
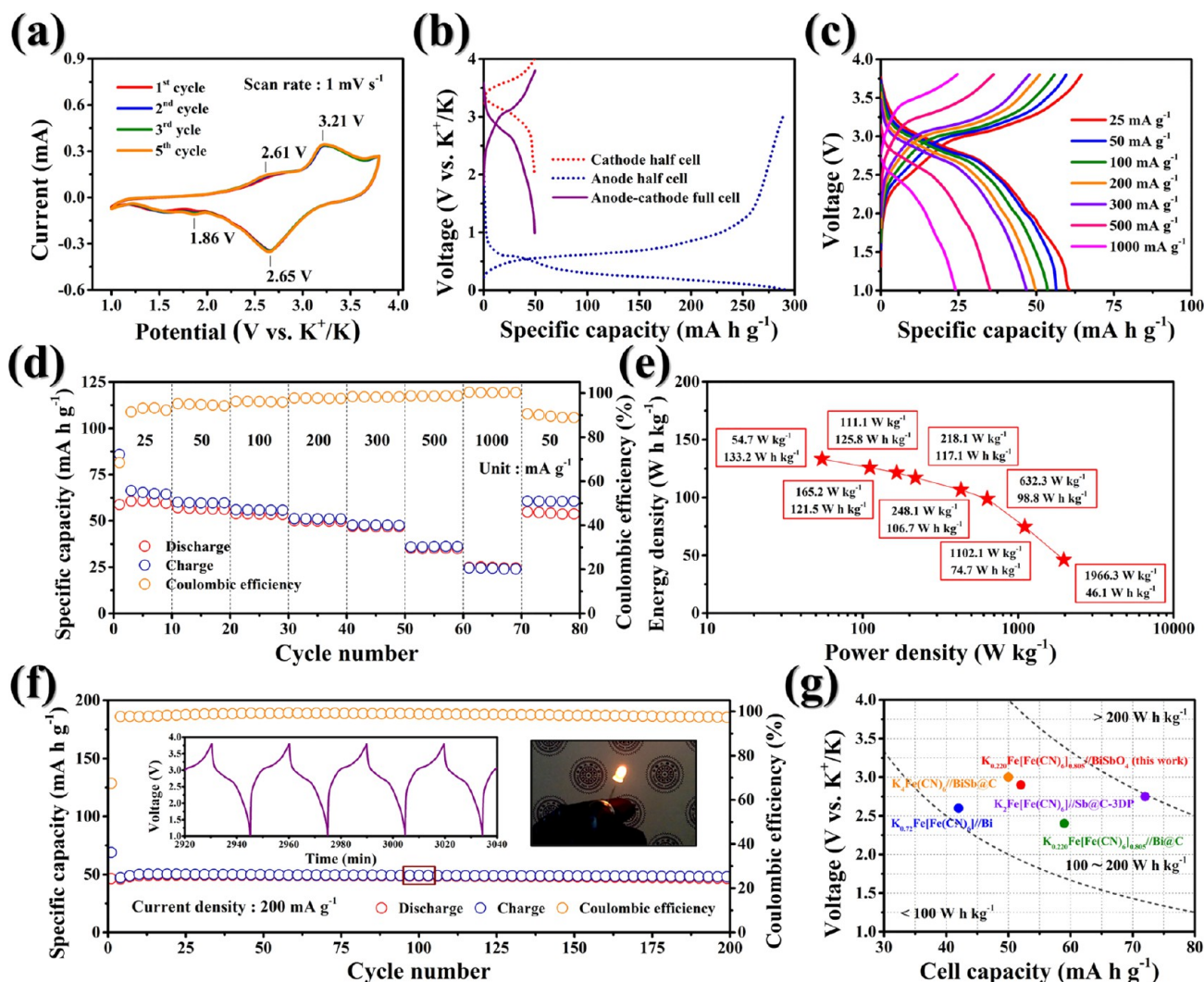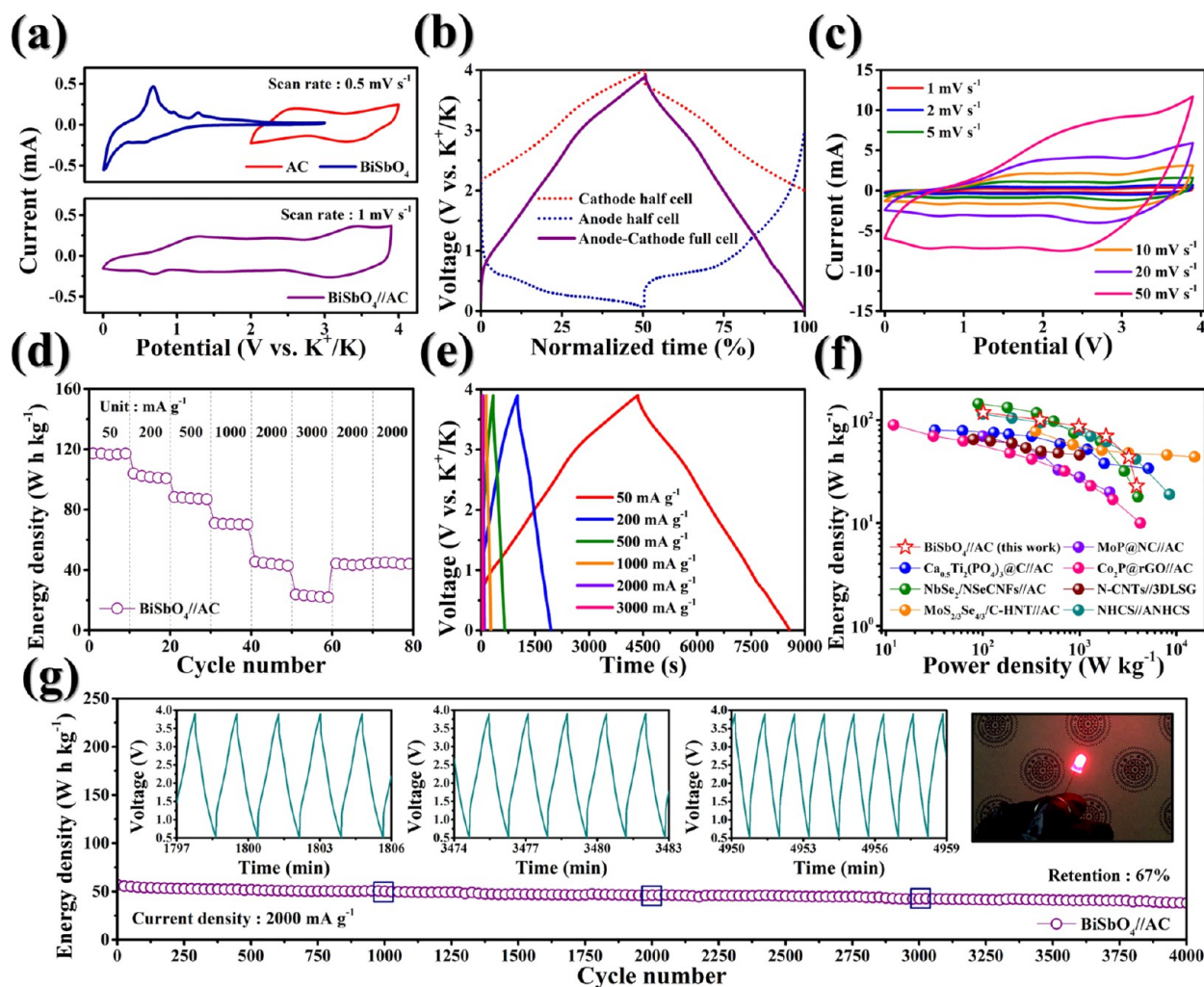
Figure 6. Electrochemical characteristics of BiSbO$_4$//PBNPs full cells for K$^+$ storage in PIBs. (a) CV profiles at a scan rate of 1 mV s^{-1} and (b) GCD curves of a half cell and a full cell. (c,d) Rate performance where the current densities are in the range from 25 to 1000 mA g^{-1} and (e) the corresponding energy densities and power densities in Ragone plots. (f) Long-term cycling performance at 200 mA g^{-1}. The insets show the continuous voltage curve and a digital picture of lighting test. (g) Comparison of the electrochemical performances of Bi- and Sb-based anode pairings with cathode in Prussian blue analogues.

voltage swing of the working electrodes, so that the thermodynamic conditions of electrode and electrolyte in half cells can be universally recognized at each current state. However, the inevitable dendrite growth in repeated electroplating also raises concerns about electrochemical stability, which hardly occurs in full cell devices.[51,52] Therefore, the cycling stability and capacity distribution cannot be directly predicted. On the contrary, considering the combined kinetics of different mechanisms in energy storage, reversible ion transport and relative voltage profiles are basically related to the capacity ratio of the anode and cathode in full cells.

The PIB full cells coupled to the cathode of Prussian blue nanoparticles (PBNPs) are fabricated, where the full cells are designated as BiSbO$_4$//PBNPs. PBNPs are synthesized *via* the coprecipitation method under continuous stirring and feeding. All of the diffraction peaks of the prepared product can be well identified as the crystal phase of Fe$_4$[Fe(CN)$_6$]$_3$ (JCPDS no. 52-1907) (Figure S14). As shown in Figures S15 and S16, CV measurements and GCD tests reveal electrochemical properties including stability and rate capability. The overlapping peaks in the CV curves and the reversibility in the GCD curves indicate

that the PBNPs half cell is in the proper voltage window of 2.0–4.0 V. Therefore, the voltage range of the full cell of BiSbO$_4$//PBNPs has been conducted under 1.0–3.8 V, and two redox couples of 1.86/2.61 and 2.65/3.21 V can be recognized with high reversibility (Figure 6a). In Figure 6b, the typical GCD curve of BiSbO$_4$//PBNPs full cells at 200 mA g^{-1}, which are calculated based on the mass of PBNPs, delivering high reversible capacity and Coulombic efficiency compared with the theoretical value of PBNPs half cells. Note that the complete redox reaction of alloying and conversion in the anode provides a considerable specific capacity and causes a difference in quality between the anode and cathode. In particular, the plateaus in the GCD curve of BiSbO$_4$//PBNPs full cells can be distinguished with the redox peaks of CV curves. As shown in Figure 6c,d, in terms of rate capability, the BiSbO$_4$//PBNPs full cells exhibit reversible capacities of 60.9, 56.8, 55.2, 53.7, 49.9, 46.9, 35.2, and 25.2 mA h g^{-1} at the current densities of 25, 50, 75, 100, 200, 300, 500, and 1000 mA g^{-1}, respectively. It is worth mentioning that when the current density rises above 500 mA g^{-1}, an overpotential appears and causes a slight displacement of charge and discharge plateaus. Despite that, BiSbO$_4$//PBNPs full cells

Figure 7. Electrochemical characteristics of BiSbO$_4$//AC PIHCs. (a) CV curves and (b) normalized GCD curves of a half cell and a full cell. (c) Kinetic analysis measured in the CV curve at the scan rates from 1 to 50 mV s^{-1}. (d,e) Rate performance at the current densities range from 50 to 3000 mA g^{-1}. (f) Ragone plots of the BiSbO$_4$//AC PIHCs in comparison with the reported PIHCs. (g) Long-term cycling performance at 2000 mA g^{-1}: the retention capacity after for 4000 cycles is 67%. The insets present the pseudocapacitive profile of a BiSbO$_4$//AC PIHC and the demonstration digital picture in LED bulb lighting.

still achieve a high energy density of 133.2 W h kg^{-1} and the power density up to 1966.3 W kg^{-1} based on the total mass of BiSbO$_4$ and PBNPs (Figure 6e). Furthermore, the long-term cycling of BiSbO$_4$//PBNPs full cells at a current density of 200 mA g^{-1} shows an ultrastable capacity during 200 cycles, and the capacity retention rate relative to the 10th cycle was 96.2%. The inset illustrates the lighting test of 1.8−2.2 V orange light-emitting diodes (LED) bulb. Notably, the high Coulombic efficiencies and voltage profiles provided in the inset suggest the high reversible K$^+$ insertion/extraction between the anode and cathode in BiSbO$_4$//PBNPs full cells (Figure 6f). We also compare the electrochemical performance with the results of the reported literature, in which the composition are cathode of Prussian blue analogues and anode of antimony and bismuth type materials.[53−56] The cell capacities based on the total mass of the anode and cathode materials and working voltages are illustrated in Figure 6g. We believe the overall cell capacity of BiSbO$_4$//PBNPs full cells can be further improved by pairing with other cathodes of Prussian blue analogues with higher theoretical capacity, thereby strengthening the energy density while maintaining the power density as a constant. Nevertheless, it is noteworthy that the excellent performance of BiSbO$_4$//

PBNPs full cells is in good agreement with the contribution of alloying and conversion in K$^+$ storage in half cells, highlighting the practical application prospects for advanced energy storage devices.

PIHCs composed of a BiSbO$_4$ anode and a commercial activated carbon (AC) cathode (designated as BiSbO$_4$//AC) are assembled in an asymmetrical device, which is based on the alloying/dealloying of K$^+$ on the anode side and adsorption/desorption of FSI$^-$ at the cathode side. The AC was used as is, without any modification, which brings a high Brunauer−Emmett−Teller (BET) surface area of 1467.43 m^2 g^{-1} in mesopores (Figure S17). Specifically, given that related work in FIS-based electrolytes has revealed that aluminum foil attrition occurs when the working voltage is higher 4.0 V, the voltage window of AC half cells should be adjusted between 2.0 and 4.0 V.[57] In Figures S18 and S19, the CV curve and the cycle performance of the AC half cells are examined and deliver a specific capacity of 47.6 mA h g^{-1} at a current density of 50 mA g^{-1}, comparable to other carbonaceous materials in the cathode. Figure 7a shows the individual redox peaks of half cells and full cells, achieving appropriate synergistic effects in the alloying and adsorption mechanisms, with a higher cutoff potential of 3.9 V,

which is a crucial factor to significantly reinforce the energy density (E) and power density (P) considering the integral and convert formula

$$E = I \int_{t_1}^{t_2} V(t)dt/m = P \times t$$

where I and t are the constant current and period of discharge process and m is the total mass loading of anode and cathode. In order to optimize the electrochemical performance of PIHCs, the mass proportion of the anode to the cathode has been adjusted to a ratio of 1, 1.5, 2, and 3, where the equivalent configuration clearly demonstrates the best performing of the Coulombic efficiency within 1000 cycles (Figure S20). Therefore, based on a sufficient anode to cathode mass ratio of 1, the BiSbO$_4$//AC full cells maintains a quasi-rectangular profile even at high operating voltages without noticeable voltage polarization, which is different from the sharp redox peaks in BiSbO$_4$ half cells. It indicates a typical capacitor-like behavior for SCs. The corresponding GCD curves are also provided in Figure 7b, showing that the anode and cathode are consistent with the reasonable displacement of the voltage plateau. Unlike common linear features in ideal SCs, the slight change in slope in the 3 V range can be attributed to the Faradaic and non-Faradaic features between the alloying-type BiSbO$_4$ anode and adsorption-type AC cathode, which is consistent with the plateaus in the CV curve. Furthermore, kinetics analysis was also carried out by CV measurement at high scan rates (Figure 7c). It is worth noting that the proportional increase shown by the peak current has no obvious overpotential shifting, indicating that the pseudocapacitive in BiSbO$_4$//AC full cells is highly dominated (Figure S21). As shown in Figure 7d, based on the total mass of BiSbO$_4$ and AC, the BiSbO$_4$//AC full cells can currently display the energy densities of 117.9, 102.4, 87.6, 70.5, 44.1, and 23.2 W h kg^{-1} at the current densities of 50, 200, 500, 1000, 2000, and 3000 mA g^{-1}, which are usually equivalent to power densities of 100.5, 395.4, 987.6, 1881.5, 3262.6, and 3932.2 W kg^{-1}, respectively. In particular, the GCD curves at different current densities show that the remaining plateau during the charge process is about 3.2 V and that during discharge process is about 2.9 V, which is consistent with the CV results at various scan rates (Figure 7e). Meanwhile, the Ragone plots based on the energy density and power density of BiSbO$_4$//AC PIHC and other alloying-based hybrid PIHCs, including MoP@NC//AC,[58] Co$_2$P@rGO//AC,[59] Ca$_{0.5}$Ti$_2$(PO$_4$)$_3$@C//AC,[60] NbSe$_2$/NSeCNFs//AC,[61] MoS$_{2/3}$Se$_{4/3}$/C-HNT//AC,[62] and carbonaceous-based capacitors, such as N-CNT//3DLSG and NHCS//ANHCS,[63,64] are presented in Figure 7f. The BiSbO$_4$//AC PIHC exhibits comparable electrochemical properties with the recently reported PIHCs. In addition, as shown in Figure 7g, the long-term cycling of BiSbO$_4$//AC PIHCs can even achieve 4000 cycles at 2000 mA g^{-1}, and the energy density retention is 67%. The insets not only demonstrate the lighting test of a red LED bulb with a working voltage of 1.8−2.2 V but also present the voltage curve of the BiSbO$_4$//AC full cells in certain periods, where the voltage range has been adjusted from 0.5 to 3.9 V, thereby offsetting the unfavorable overpotential of IR drop at high current density. The prominent achievement of BiSbO$_4$//AC full cells should be ascribed to the merits, including proper adsorption, adequacy of active sites, high reversible capacity associated with the Faradaic process, and robust durability in rapid ion transport.

CONCLUSIONS

In conclusion, the introduction of BiSbO$_4$ nanonetwork constructs advanced the architecture of metal oxide and proposes the synergistic role of facet and structural engineering to enhance metal oxide on K$^+$ storage. Kinetic analyses and DFT calculations were carried out to thoroughly study the effect of exposed facets for the enhanced ion diffusion transport. The synergistic facet and architecture engineering of the metal oxides enable the highly reversible dual conversion-alloying mechanism of BiSbO$_4$, *i.e.*, the coexistence of phase evolution of (Bi, Sb) alloying and reversible formation of KO$_2$, and can thereby deliver excellent long-term and high rate performance of K$^+$ storage. Importantly, the BiSbO$_4$ network can be used directly as implemented in PIBs and PIHCs full cells, indicating that it has favorable conditions for ultrastable cycles with high energy density and power density in the field of energy storage. For different energy storage technologies, such as batteries and capacitors, there must be a big trade-off between energy density and power density, which have been pointed out in several studies, especially for carbonaceous materials.[65,66] From the Ragone plots in Figure S22, BiSbO$_4$ can exhibit excellent performance in both energy density and power density with pairing with the same counter electrodes of PBNPs and AC. This feature indicates that the energy-storage mechanism of dual conversion-alloying can not only improve the electrochemical performance but also maintain a relatively great stability in the case of high current density. Moreover, the BiSbO$_4$//AC PIHCs can even achieve a reversible cycling in less than 1 min, which indicates the mechanism of battery behavior can be realized in rapid charge transfer and beyond the limitation in conventional batteries. This work proposes a promising way to design advanced hierarchical nanostructures, which may be applicable to any ternary or binary conversion nanomaterials used in PIB and PIHC or a wide range of energy storage.

METHODS

Chemical Details. All reagents in this work are commercially available. Bismuth(III) nitrate pentahydrate (Bi(NO$_3$)$_3$·5H$_2$O, reagent grade, 98%), hexadecyltrimethylammonium bromide (CTAB, for molecular biology, 99%), sodium carboxymethyl cellulose (NaCMC, average $M_w \sim$ 700000), poly(acrylic acid) (PAA, average $M_w \sim$ 3000000), 1-methyl-2-pyrrolidinone (NMP, anhydrous, 99.5%), potassium (chunks, in mineral oil, 98%), and dimethyl carbonate (DMC, anhydrous, 99%) were purchased from Sigma-Aldrich. Antimony(III) oxide (Sb$_2$O$_3$, 99%), bismuth(III) oxide (Bi$_2$O$_3$, 99%), and iron(III) chloride (FeCl$_3$, anhydrous, 98%) were purchased from Alfa Aesar. Hydrochloric acid (HCl, ACS reagent, 37%) was purchased from Honeywell Fluka. Sodium hydroxide (NaOH, pellets, ACS reagent) and potassium hexacyanoferrate (II) trihydrate (K$_4$Fe-(CN)$_6$·3H$_2$O, 98.5%) were purchased from J.T. Baker. Absolute ethanol was purchased from Echo Chemical. Active carbon (AC) was purchased from Kuraray Chemical. Potassium bis(fluorosulfonyl) imide (KFSI, 97%) was purchased from Combi-Blocks. Super-P carbon black, polyvinylidene fluoride (PVDF), and CR2032 coin-type cells were purchased from Shining Energy. Glass fiber was purchased from Advantec Group. Copper foil and aluminum foil were purchased from Chang-Chun Group. Deionized water was produced by a Milli-Q Direct pure water system.

Material Preparations. *Synthesis of BiSbO$_4$ Powders.* On the basis of previous study, the as-prepared BiSbO$_4$ powders were obtained from solid-state reaction at high temperature.[67] Bi$_2$O$_3$ (0.4659 g) and Sb$_2$O$_3$ (0.2915 g) were added into the stainless steel and rotated at 150 rpm for 30 min in the Planetary Ball Mill 100 machine. The well-mixed powder was transferred into a ceramic boat and calcined at 600 °C for

24 h inside a furnace. Thereafter, the agglomerated solid was reground into powder and recalcined at 850 °C for 12 h.

Synthesis of BiSbO₄ Nanorods. The as-prepared $BiSbO_4$ nanorods were obtained by the hydrothermal method, which has been investigated in previous research.[68] $Bi(NO_3)_3 \cdot 5H_2O$ (0.9701 g) and Sb_2O_3 (0.2915 g) were added into a serum bottle sequentially with 20 mL of deionized water with constant stirring (500 rpm) for 30 min. Thereafter, addition of 1 mL of 2 M aqueous NaOH solution and 8 mL deionized water was carried out to tune the pH value and fill up the solution to 30 mL in volume. The mixture was treated at 210 °C for 24 h in a Teflon-lined autoclave reactor. The obtained sediment was collected by centrifugation (5 min per cycle at 8500 rpm) three times using absolute ethanol and deionized water with volume ratio of 5:4.

Synthesis of BiSbO₄ Nanonetworks. In a typical synthesis, the aqueous CTAB solution was prepared by adding 0.075 g of CTAB into a serum bottle with 25 mL of deionized water *via* constant stirring (500 rpm) for 30 min. Thereafter, 0.4851 g $Bi(NO_3)_3 \cdot 5H_2O$ and 0.1458 g Sb_2O_3 were added into the serum bottle. The mixture was treated through a hydrothermal method at 170 °C for 24 h in a Teflon-lined autoclave reactor. The obtained sediment was collected by centrifugation (5 min per cycle at 8500 rpm) three times using absolute ethanol and deionized water with a volume ratio of 5:4. After being washed with 1 M HCl solution, the obtained powder was further annealed at 200 °C for 24 h in a furnace.

Synthesis of Prussian Blue Nanoparticles. Modified from a previous report, the experiment was scaled up in terms of overall yield increment.[69] $K_4Fe(CN)_6 \cdot 3H_2O$ (1.2672 g) was dissolved in 160 mL of deionized water with vigorous stirring, which was denoted as solution A. In the meantime, 0.9720 g of $FeCl_3$ was dissolved in 40 mL of deionized water and sonicated for 20 min, which was denoted as solution B. Thereafter, the solution B was dropwise added into solution A by a KDS Legacy Series syringe pump with continuous stirring, and the dark blue precipitation formed immediately. The suspension was stirred for 2 h and further aged for 12 h. The obtained sediment was collected by centrifugation (5 min per cycle at 11500 rpm) two times using deionized water and dried at 80 °C in a vacuum oven for 12 h.

Electrochemical Measurements. *Preparation of BiSbO₄ Electrodes.* These electrodes were prepared by mixing the active material (70%), super-P carbon black (20%), PAA (5%), and NaCMC (5%) in absolute ethanol and DI water, which was added into a sample vial and stirred overnight to form a uniform slurry. The homogeneous slurry was coated onto the copper foil and dried inside a furnace at 150 °C under argon gas to remove the residual solvent. The mass loading of active material in $BiSbO_4$ electrodes is 1.0−1.2 mg cm⁻² with 0.1 μg resolution (Sartorius SE2).

Potassium Ion Half Cells Assembly of Anode Materials. The electrochemical performance of the electrodes was tested using CR2032 coin-type half cells with handmade potassium metal foil as the counter electrode. The electrolyte used in the cells was 1 M KFSI in DMC. The cells were assembled in an argon-filled glovebox with both the moisture and the oxygen content below 1 ppm (M. Braun UNILAB). The CV and EIS curves were obtained on Bio-Logic-Science Instruments, VMP3 workstation. Galvanostatic discharge−charge tests were evaluated by NEWARE CT-4000 battery measurement system from 0.01 to 3.0 V *vs* K⁺/K. Galvanostatic intermittent titration technique (GITT) measurements were performed by charging/discharging the cells for 10 min at 100 mA g⁻¹ followed by a 1 h relaxation.

Preparation of AC Electrodes. These electrodes were prepared by mixing the AC (80%), super-P carbon black (10%), and PVDF (10%) in NMP solvent, which was added into an ointment jar and put into a Thinky ARE-310 planetary centrifugal mixer to form a uniform slurry. Thereafter, the homogeneous slurry was coated onto the aluminum foil and dried inside a furnace at 150 °C under argon gas to remove the residual solvent. The average active material loading for the AC is 1.5−2.0 mg cm⁻² with 0.1 μg resolution (Sartorius SE2).

Preparation of PBNP Electrodes. These electrodes were prepared by mixing the PBNPs (80%), super-P carbon black (10%), and PVDF (10%) in NMP solvent, which was added into a plastic jar and put into an MTI MSK-SFM-12 M ball mill machine rotated at 350 rpm for 15 min. The homogeneous slurry was coated on to the aluminum foil and dried inside a furnace at 150 °C under argon gas to remove the residual solvent. The average active material loading for the PBNPs is 2.5−3.0 mg cm⁻² with 0.1 μg resolution (Sartorius SE2).

Potassium Ion Half Cell Assembly of Cathode Materials. The electrochemical performance of the electrodes was tested in the CR2032 coin-type half cells with the handmade potassium metal foil as the counter electrode. The electrolyte used in the cells was 1 M KFSI in DMC. The cells were assembled in an argon-filled glovebox with both the moisture and the oxygen content bellow 1 ppm (M. Braun UNILAB). Galvanostatic discharge−charge tests were evaluated by NEWARE CT-4000 battery measurement system from 2.0 to 4.0 V vs. K⁺/K.

Coin-Type Full Cells for Batteries. The CR2032 coin-type full cell for the battery was assembled by using $BiSbO_4$ (~0.5 mg cm⁻²) as anode and PBNPs (2.5−3.0 mg cm⁻²) as cathode with overall mass ratio of 6 under argon environment. Both $BiSbO_4$ and PBNP electrodes were preactivated for several cycles before the full cell assembly, and 1 M KFSI in DMC was used as electrolyte. The CV curves were obtained on Bio-Logic-Science Instruments, VMP3 workstation. Galvanostatic discharge−charge tests were evaluated by a NEWARE CT-4000 battery measurement system from 1.0 to 3.8 V *vs* K⁺/K.

Coin-Type Full Cells for Hybrid Capacitors. The CR2032 coin-type full cell for the hybrid capacitor was assembled by using $BiSbO_4$ (1.5−2.0 mg cm⁻²) as anode and AC (1.5−2.0 mg cm⁻²) as cathode with overall mass ratio of 1 under argon environment. The $BiSbO_4$ electrodes were preactivated for 20 cycles at high current density before the full cell assembly, and 1 M KFSI in DMC was used as electrolyte. The CV curves were obtained on Bio-Logic-Science Instruments, VMP3 workstation. Galvanostatic discharge−charge tests were evaluated by Maccor Series 4000 battery measurement system from 0 to 3.9 V *vs* K⁺/K.

Computational Methods. The present first principle DFT calculations were performed using the Vienna *Ab initio* Simulation Package with the projector augmented wave method.[70,71] The exchange-correlation functional was treated using the generalized gradient approximation of Perdew−Burke−Ernzerhof functional.[72] The energy cutoff for the plane wave basis expansion was set to 450 eV and the force on each atom less than 0.03 eV Å⁻¹ was set for convergence criterion of geometry relaxation.15 Å vacuum was added along the z direction in order to avoid the interaction between periodic structures. The Brillouin zone integration was performed using $2 \times 2 \times 1$ k-point sampling. The self-consistent calculations apply a convergence energy threshold of 10^{-5} eV. The DFT-D3 method was employed to consider the van der Waals interaction.[73] Transition state searching was calculated using the climbing-image nudged elastic band (CI-NEB) method.[74] The adsorption energy of the K atom was calculated according to following equation

$$E_{ads} = E_{total} - E_{sub} - E_K$$

where E_{total} is the total energy of the K atom adsorbed systems, while E_{sub} and E_K are the energies of the substrate and the K atom in bulks, respectively.

ASSOCIATED CONTENT

Ⓢ Supporting Information

The Supporting Information is available free of charge at https://pubs.acs.org/doi/10.1021/acsnano.1c09863.

Experimental section; SEM images, EDS, cyclic voltammetry curves, and galvanostatic charge−discharge curve of $BiSbO_4$ nanonetworks, nanorods and $BiSbO_4$ powders; the cross-section SEM images of a $BiSbO_4$ electrode; theoretical calculation of K atom adsorption and diffusion in the facets of $BiSbO_4$; spectra of X-ray photoelectron spectroscopy at 1st cycle and 100th cycle; electrochemical performance of PBNPs half cells; N_2 adsorption−desorption isotherms for AC; electrochemical perform-

ance of AC half cells; kinetics analysis of BiSbO$_4$//AC full cell (PDF)

AUTHOR INFORMATION

Corresponding Author

Hsing-Yu Tuan − *Department of Chemical Engineering, National Tsing Hua University, Hsinchu 30013, Taiwan;* orcid.org/0000-0003-2819-2270; Phone: (886)3-571-5131; Email: hytuan@che.nthu.edu.tw

Authors

Chao-Hung Chang − *Department of Chemical Engineering, National Tsing Hua University, Hsinchu 30013, Taiwan*

Kuan-Ting Chen − *Department of Chemical Engineering, National Tsing Hua University, Hsinchu 30013, Taiwan*

Yi-Yen Hsieh − *Department of Chemical Engineering, National Tsing Hua University, Hsinchu 30013, Taiwan*

Che-Bin Chang − *Department of Chemical Engineering, National Tsing Hua University, Hsinchu 30013, Taiwan*

Complete contact information is available at:
https://pubs.acs.org/10.1021/acsnano.1c09863

Author Contributions

†C.-H.C. and K.-T.C. contributed equally to this work and share first authorship.

Notes

The authors declare no competing financial interest.

REFERENCES

(1) Lai, C.-M.; Kao, T.-L.; Tuan, H.-Y. Si Nanowires/Cu Nanowires Bilayer Fabric as a Lithium Ion Capacitor Anode with Excellent Performance. *J. Power Sources* **2018**, *379*, 261−269.

(2) Chu, H.-C.; Tuan, H.-Y. High-Performance Lithium-Ion Batteries with 1.5 μm Thin Copper Nanowire Foil as a Current Collector. *J. Power Sources* **2017**, *346*, 40−48.

(3) Ma, Y.; Chang, H.; Zhang, M.; Chen, Y. Graphene-Based Materials for Lithium-Ion Hybrid Supercapacitors. *Adv. Mater.* **2015**, *27*, 5296−5308.

(4) Choi, J. W.; Aurbach, D. Promise and Reality of Post-Lithium-Ion Batteries with High Energy Densities. *Nat. Rev. Mater.* **2016**, *1*, 1−16.

(5) Xu, J.; Dou, S.; Cui, X.; Liu, W.; Zhang, Z.; Deng, Y.; Hu, W.; Chen, Y. Potassium-Based Electrochemical Energy Storage Devices: Development Status and Future Prospect. *Energy Stor. Mater.* **2021**, *34*, 85−106.

(6) Wang, M.; Zhang, H.; Cui, J.; Yao, S.; Shen, X.; Park, T. J.; Kim, J.-K. Recent Advances in Emerging Nonaqueous K-Ion Batteries: From Mechanistic Insights to Practical Applications. *Energy Stor. Mater.* **2021**, *39*, 305−346.

(7) Yin, H.; Han, C.; Liu, Q.; Wu, F.; Zhang, F.; Tang, Y. Recent Advances and Perspectives on the Polymer Electrolytes for Sodium/Potassium-Ion Batteries. *Small* **2021**, *17*, 2006627.

(8) Li, X.; Ou, X.; Tang, Y. 6.0 V High-Voltage and Concentrated Electrolyte toward High Energy Density K-Based Dual-Graphite Battery. *Adv. Energy Mater.* **2020**, *10*, 2002567.

(9) Liu, S.; Mao, J.; Zhang, Q.; Wang, Z.; Pang, W. K.; Zhang, L.; Du, A.; Sencadas, V.; Zhang, W.; Guo, Z. An Intrinsically Non-Flammable Electrolyte for High-Performance Potassium Batteries. *Angew. Chem., Int. Ed.* **2020**, *59*, 3638−3644.

(10) Zhang, X.; Meng, J.; Wang, X.; Xiao, Z.; Wu, P.; Mai, L. Comprehensive Insights into Electrolytes and Solid Electrolyte Interfaces in Potassium-Ion Batteries. *Energy Stor. Mater.* **2021**, *38*, 30−49.

(11) Liu, X.; Elia, G. A.; Qin, B.; Zhang, H.; Ruschhaupt, P.; Fang, S.; Varzi, A.; Passerini, S. High-Power Na-Ion and K-Ion Hybrid Capacitors Exploiting Cointercalation in Graphite Negative Electrodes. *ACS Energy Lett.* **2019**, *4*, 2675−2682.

(12) Zhao, J.; Burke, A. F. Electrochemical Capacitors: Materials, Technologies and Performance. *Energy Stor. Mater.* **2021**, *36*, 31−55.

(13) Zhang, W.; Yin, J.; Wang, W.; Bayhan, Z.; Alshareef, H. N. Status of Rechargeable Potassium Batteries. *Nano Energy* **2021**, *83*, 105792.

(14) Wang, J.; Fan, L.; Liu, Z.; Chen, S.; Zhang, Q.; Wang, L.; Yang, H.; Yu, X.; Lu, B. *In Situ* Alloying Strategy for Exceptional Potassium Ion Batteries. *ACS Nano* **2019**, *13*, 3703−3713.

(15) Wang, S.; Xiong, P.; Guo, X.; Zhang, J.; Gao, X.; Zhang, F.; Tang, X.; Notten, P. H.; Wang, G. A Stable Conversion and Alloying Anode for Potassium-Ion Batteries: A Combined Strategy of Encapsulation and Confinement. *Adv. Funct. Mater.* **2020**, *30*, 2001588.

(16) Verma, R.; Didwal, P. N.; Nguyen, A.-G.; Park, C.-J. SnSe Nanocomposite Chemically-Bonded with Carbon-Coating as an Anode Material for K-Ion Batteries with Outstanding Capacity and Cyclability. *Chem. Eng. J.* **2021**, *421*, 129988.

(17) Chen, K.-T.; Chong, S.; Yuan, L.; Yang, Y.-C.; Tuan, H.-Y. Conversion-Alloying Dual Mechanism Anode: Nitrogen-Doped Carbon-Coated Bi2Se3 Wrapped with Graphene for Superior Potassium-Ion Storage. *Energy Stor. Mater.* **2021**, *39*, 239−249.

(18) Wei, C.; Tao, Y.; Fei, H.; An, Y.; Tian, Y.; Feng, J.; Qian, Y. Recent Advances and Perspectives in Stable and Dendrite-Free Potassium Metal Anodes. *Energy Stor. Mater.* **2020**, *30*, 206−227.

(19) An, Y.; Tian, Y.; Ci, L.; Xiong, S.; Feng, J.; Qian, Y. Micron-Sized Nanoporous Antimony with Tunable Porosity for High-Performance Potassium-Ion Batteries. *ACS Nano* **2018**, *12*, 12932−12940.

(20) Zhang, Y.; Li, L.; Su, H.; Huang, W.; Dong, X. Binary Metal Oxide: Advanced Energy Storage Materials in Supercapacitors. *J. Mater. Chem. A* **2015**, *3*, 43−59.

(21) Nguyen, T.; Montemor, M. d. F. Metal Oxide and Hydroxide-Based Aqueous Supercapacitors: From Charge Storage Mechanisms and Functional Electrode Engineering to Need-Tailored Devices. *Adv. Sci.* **2019**, *6*, 1801797.

(22) An, Y.; Fei, H.; Zeng, G.; Ci, L.; Xi, B.; Xiong, S.; Feng, J. Commercial Expanded Graphite as a Low-Cost, Long-Cycling Life Anode for Potassium-Ion Batteries with Conventional Carbonate Electrolyte. *J. Power Sources* **2018**, *378*, 66−72.

(23) An, C.; Zhang, Y.; Guo, H.; Wang, Y. Metal Oxide-Based Supercapacitors: Progress and Prospectives. *Nanoscale Adv.* **2019**, *1*, 4644−4658.

(24) Jiang, J.; Li, Y.; Liu, J.; Huang, X.; Yuan, C.; Lou, X. W. Recent Advances in Metal Oxide-Based Electrode Architecture Design for Electrochemical Energy Storage. *Adv. Mater.* **2012**, *24*, 5166−5180.

(25) Wang, J.; Wang, B.; Liu, Z.; Fan, L.; Zhang, Q.; Ding, H.; Wang, L.; Yang, H.; Yu, X.; Lu, B. Nature of Bimetallic Oxide Sb2MoO6/rGO Anode for High-Performance Potassium-Ion Batteries. *Adv. Sci.* **2019**, *6*, 1900904.

(26) Li, J.; Zhuang, N.; Xie, J.; Li, X.; Zhuo, W.; Wang, H.; Na, J. B.; Li, X.; Yamauchi, Y.; Mai, W. K-Ion Storage Enhancement in Sb2O3/Reduced Graphene Oxide Using Ether-Based Electrolyte. *Adv. Energy Mater.* **2020**, *10*, 1903455.

(27) Adekoya, D.; Chen, H.; Hoh, H. Y.; Gould, T.; Balogun, M.-S. J. T.; Lai, C.; Zhao, H.; Zhang, S. Hierarchical Co3O4@N-Doped Carbon Composite as an Advanced Anode Material for Ultrastable Potassium Storage. *ACS Nano* **2020**, *14*, 5027−5035.

(28) Liang, H.; Zhang, Y.; Hao, S.; Cao, L.; Li, Y.; Li, Q.; Chen, D.; Wang, X.; Guo, X.; Li, H. Fast Potassium Storage in Porous CoV2O6 Nanosphere@Graphene Oxide towards High-Performance Potassium-Ion Capacitors. *Energy Stor. Mater.* **2021**, *40*, 250−258.

(29) Luo, Y.; Wang, C.; Wang, X. Fast Energy Storage Performance of CoFe2O4/CNTs Hybrid Aerogels for Potassium Ion Battery. *J. Colloid Interface Sci.* **2021**, *600*, 820−827.

(30) Wu, J.; Liu, S.; Rehman, Y.; Huang, T.; Zhao, J.; Gu, Q.; Mao, J.; Guo, Z. Phase Engineering of Nickel Sulfides to Boost Sodium- and Potassium-Ion Storage Performance. *Adv. Funct. Mater.* **2021**, *31*, 2010832.

(31) Dathar, G. K. P.; Sheppard, D.; Stevenson, K. J.; Henkelman, G. Calculations of Li-Ion Diffusion in Olivine Phosphates. *Chem. Mater.* **2011**, *23*, 4032−4037.

(32) Pan, L.; Zhang, Y.; Lu, F.; Du, Y.; Lu, Z.; Yang, Y.; Ye, T.; Liang, Q.; Bando, Y.; Wang, X. Exposed Facet Engineering Design of Graphene-SnO2 Nanorods for Ultrastable Li-Ion Batteries. *Energy Stor. Mater.* **2019**, *19*, 39−47.

(33) An, Q.; Wei, Q.; Zhang, P.; Sheng, J.; Hercule, K. M.; Lv, F.; Wang, Q.; Wei, X.; Mai, L. Three-Dimensional Interconnected Vanadium Pentoxide Nanonetwork Cathode for High-Rate Long-Life Lithium Batteries. *Small* **2015**, *11*, 2654−2660.

(34) Xiao, K.; Xia, L.; Liu, G.; Wang, S.; Ding, L.-X.; Wang, H. Honeycomb-Like NiMoO4 Ultrathin Nanosheet Arrays for High-Performance Electrochemical Energy Storage. *J. Mater. Chem. A* **2015**, *3*, 6128−6135.

(35) Zhang, J.; Yuan, H.; Huang, Y.; Kan, S.; Wu, Y.; Bu, M.; Liu, Y.; He, P.; Liu, H. Engineering Sodium-Rich Manganese Oxide with Robust Tunnel Structure for High-Performance Sodium-Ion Battery Cathode Application. *Chem. Eng. J.* **2021**, *417*, 128097.

(36) Zhou, J.; Zheng, C.; Yang, Y.; Guo, L. Facile Synthesis of Novel Nest-Shaped Sb2O3Micro/Nanostructures and Their Optical Properties. *RSC Adv.* **2016**, *6*, 89799−89802.

(37) Errandonea, D.; Muñoz, A.; Rodríguez-Hernández, P.; Gomis, O.; Achary, S. N.; Popescu, C.; Patwe, S. J.; Tyagi, A. K. High-Pressure Crystal Structure, Lattice Vibrations, and Band Structure of BiSbO4. *Inorg. Chem.* **2016**, *55*, 4958−4969.

(38) Schuhl, Y.; Baussart, H.; Delobel, R.; Le Bras, M.; Leroy, J.-M.; Gengembre, L.; Grimblot, J. Study of Mixed-Oxide Catalysts Containing Bismuth, Vanadium and Antimony. Preparation, Phase Composition, Spectroscopic Characterization and Catalytic Oxidation of Propene. *J. Chem. Soc., Faraday Trans. 1 F* **1983**, *79*, 2055−2069.

(39) Wen, J.; Xu, L.; Wang, J.; Xiong, Y.; Ma, J.; Jiang, C.; Cao, L.; Li, J.; Zeng, M. Lithium and Potassium Storage Behavior Comparison for Porous Nanoflaked Co3O4 Anode in Lithium-Ion and Potassium-Ion Batteries. *J. Power Sources* **2020**, *474*, 228491.

(40) Cao, K.; Liu, H.; Li, W.; Han, Q.; Zhang, Z.; Huang, K.; Jing, Q.; Jiao, L. CuO Nanoplates for High-Performance Potassium-Ion Batteries. *Small* **2019**, *15*, 1901775.

(41) Hu, J.; Xie, Y.; Zheng, J.; Lai, Y.; Zhang, Z. Unveiling Nanoplates-Assembled Bi2MoO6Microsphere as a Novel Anode Material for High Performance Potassium-Ion Batteries. *Nano Res.* **2020**, *13*, 2650−2657.

(42) Huang, R.; Lin, J.; Zhou, J.; Fan, E.; Zhang, X.; Chen, R.; Wu, F.; Li, L. Hierarchical Triple-Shelled MnCo2O4 Hollow Microspheres as High-Performance Anode Materials for Potassium-Ion Batteries. *Small* **2021**, *17*, 2007597.

(43) Zhu, H.; Liu, T.; Peng, L.; Yao, W.; Kang, F.; Shu, J.; Yang, C. A Compact Bi2WO6Microflowers Anode for Potassium-Ion Storage: Taming a Sequential Phase Evolution toward Stable Electrochemical Cycling. *Nano Energy* **2021**, *82*, 105784.

(44) Wang, J.; Polleux, J.; Lim, J.; Dunn, B. Pseudocapacitive Contributions to Electrochemical Energy Storage in TiO2 (Anatase) Nanoparticles. *J. Phys. Chem. C* **2007**, *111*, 14925−14931.

(45) Augustyn, V.; Come, J.; Lowe, M. A.; Kim, J. W.; Taberna, P.-L.; Tolbert, S. H.; Abruña, H. D.; Simon, P.; Dunn, B. High-Rate Electrochemical Energy Storage through Li+ Intercalation Pseudocapacitance. *Nat. Mater.* **2013**, *12*, 518−522.

(46) Hsieh, Y.-Y.; Chen, K.-T.; Tuan, H.-Y. A Synergetic SnSb-Amorphous Carbon Composites Prepared from Polyesterification Process as an Ultrastable Potassium-Ion Battery Anode. *Chem. Eng. J.* **2021**, *420*, 130451.

(47) Chen, K.-T.; Tuan, H.-Y. Bi-Sb Nanocrystals Embedded in Phosphorus as High-Performance Potassium Ion Battery Electrodes. *ACS Nano* **2020**, *14*, 11648−11661.

(48) Chen, K.-T.; Yang, Y.-C.; Lyu, L.-M.; Lu, M.-Y.; Tuan, H.-Y. *In Situ* Formed Robust Submicron-Sized Nanocrystalline Aggregates Enable Highly-Reversible Potassium Ion Storage. *Nano Energy* **2021**, *88*, 106233.

(49) Zhang, X.; Wang, S.; Xue, C.; Xin, C.; Lin, Y.; Shen, Y.; Li, L.; Nan, C. W. Self-Suppression of Lithium Dendrite in All-Solid-State Lithium Metal Batteries with Poly(vinylidene Difluoride)-Based Solid Electrolytes. *Adv. Mater.* **2019**, *31*, 1806082.

(50) Ren, X.; Yu, D.; Yuan, L.; Bai, Y.; Huang, K.; Liu, J.; Feng, S. *In Situ* Exsolution of Ag From AgBiS2 Nanocrystal Anode Boosting High-Performance Potassium-Ion Batteries. *J. Mater. Chem. A* **2020**, *8*, 15058−15065.

(51) Min, X.; Xiao, J.; Fang, M.; Wang, W. A.; Zhao, Y.; Liu, Y.; Abdelkader, A. M.; Xi, K.; Kumar, R. V.; Huang, Z. Potassium-Ion Batteries: Outlook on Present and Future Technologies. *Energy Environ. Sci.* **2021**, *14*, 2186−2243.

(52) Wu, Y.; Sun, Y.; Tong, Y.; Liu, X.; Zheng, J.; Han, D.; Li, H.; Niu, L. Recent Advances in Potassium-Ion Hybrid Capacitors: Electrode Materials, Storage Mechanisms and Performance Evaluation. *Energy Stor. Mater.* **2021**, *41*, 108−132.

(53) Lei, K.; Wang, C.; Liu, L.; Luo, Y.; Mu, C.; Li, F.; Chen, J. A Porous Network of Bismuth Used as the Anode Material for High-Energy-Density Potassium-Ion Batteries. *Angew. Chem.* **2018**, *130*, 4777−4781.

(54) He, X.-D.; Liu, Z.-H.; Liao, J.-Y.; Ding, X.; Hu, Q.; Xiao, L.-N.; Wang, S.; Chen, C.-H. A Three-Dimensional Macroporous Antimony@Carbon Composite as a High-Performance Anode Material for Potassium-Ion Batteries. *J. Mater. Chem. A* **2019**, *7*, 9629−9637.

(55) Xiong, P.; Wu, J.; Zhou, M.; Xu, Y. Bismuth-Antimony Alloy Nanoparticle@Porous Carbon Nanosheet Composite Anode for High-Performance Potassium-Ion Batteries. *ACS Nano* **2020**, *14*, 1018−1026.

(56) Xiang, X.; Liu, D.; Zhu, X.; Fang, K.; Zhou, K.; Tang, H.; Xie, Z.; Li, J.; Zheng, H.; Qu, D. Evaporation-Induced Formation of Hollow Bismuth@N-Doped Carbon Nanorods for Enhanced Electrochemical Potassium Storage. *Appl. Surf. Sci.* **2020**, *514*, 145947.

(57) McOwen, D. W.; Seo, D. M.; Borodin, O.; Vatamanu, J.; Boyle, P. D.; Henderson, W. A. Concentrated Electrolytes: Decrypting Electrolyte Properties and Reassessing Al Corrosion Mechanisms. *Energy Environ. Sci.* **2014**, *7*, 416−426.

(58) Zong, W.; Chui, N.; Tian, Z.; Li, Y.; Yang, C.; Rao, D.; Wang, W.; Huang, J.; Wang, J.; Lai, F. Ultrafine MoP Nanoparticle Splotched Nitrogen-Doped Carbon Nanosheets Enabling High-Performance 3D-Printed Potassium-Ion Hybrid Capacitors. *Adv. Sci.* **2021**, *8*, 2004142.

(59) Wang, Y.; Zhang, Z.; Wang, G.; Yang, X.; Sui, Y.; Du, F.; Zou, B. Ultrafine Co2P Nanorods Wrapped by Graphene Enable a Long Cycle Life Performance for a Hybrid Potassium-Ion Capacitor. *Nanoscale Horiz.* **2019**, *4*, 1394−1401.

(60) Zhang, Z.; Li, M.; Gao, Y.; Wei, Z.; Zhang, M.; Wang, C.; Zeng, Y.; Zou, B.; Chen, G.; Du, F. Fast Potassium Storage in Hierarchical Ca0.5Ti2(PO4)3@C Microspheres Enabling High-Performance Potassium-Ion Capacitors. *Adv. Funct. Mater.* **2018**, *28*, 1802684.

(61) Chen, M.; Wang, L.; Sheng, X.; Wang, T.; Zhou, J.; Li, S.; Shen, X.; Zhang, M.; Zhang, Q.; Yu, X. An Ultrastable Nonaqueous Potassium-Ion Hybrid Capacitor. *Adv. Funct. Mater.* **2020**, *30*, 2004247.

(62) Gao, J.; Wang, G.; Liu, Y.; Li, J.; Peng, B.; Jiao, S.; Zeng, S.; Zhang, G. Ternary Molybdenum Sulfoselenide Based Hybrid Nanotubes Boost Potassium-Ion Diffusion Kinetics for High Energy/Power Hybrid Capacitors. *J. Mater. Chem. A* **2020**, *8*, 13946−13954.

(63) Moussa, M.; Al-Bataineh, S. A.; Losic, D.; Dubal, D. P. Engineering of High-Performance Potassium-Ion Capacitors Using Polyaniline-Derived N-Doped Carbon Nanotubes Anode and Laser Scribed Graphene Oxide Cathode. *Appl. Mater. Today* **2019**, *16*, 425−434.

(64) Qiu, D.; Guan, J.; Li, M.; Kang, C.; Wei, J.; Li, Y.; Xie, Z.; Wang, F.; Yang, R. Kinetics Enhanced Nitrogen-Doped Hierarchical Porous Hollow Carbon Spheres Boosting Advanced Potassium-Ion Hybrid Capacitors. *Adv. Funct. Mater.* **2019**, *29*, 1903496.

(65) Fan, L.; Lin, K.; Wang, J.; Ma, R.; Lu, B. A Nonaqueous Potassium-Based Battery-Supercapacitor Hybrid Device. *Adv. Mater.* **2018**, *30*, 1800804.

(66) Moyer, K.; Donohue, J.; Ramanna, N.; Cohn, A. P.; Muralidharan, N.; Eaves, J.; Pint, C. L. High-Rate Potassium Ion and Sodium Ion Batteries by Co-Intercalation Anodes and Open Framework Cathodes. *Nanoscale* **2018**, *10*, 13335−13342.

(67) Lin, X. P.; Huang, F. Q.; Wang, W. D.; Zhang, K. L. A Novel Photocatalyst BiSbO4 for Degradation of Methylene Blue. *Appl. Catal., A* **2006**, *307*, 257−262.

(68) Wu, J.; Huang, F.; Lü, X.; Chen, P. One-Pot Synthesis of BiSbO4 Nanophotocatalyst with Enhanced Visible-Light Performance. *CrystEngComm* **2011**, *13*, 3920−3924.

(69) Zhang, C.; Xu, Y.; Zhou, M.; Liang, L.; Dong, H.; Wu, M.; Yang, Y.; Lei, Y. Potassium Prussian Blue Nanoparticles: A Low-Cost Cathode Material for Potassium-Ion Batteries. *Adv. Funct. Mater.* **2017**, *27*, 1604307.
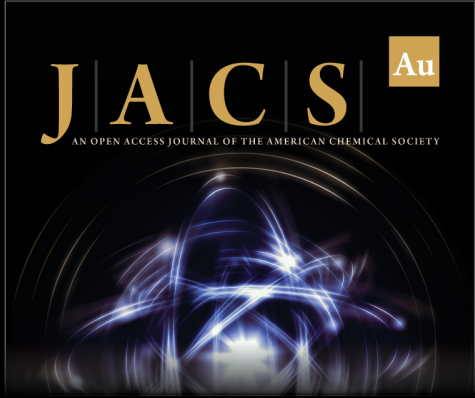
(70) Blöchl, P. E. Projector Augmented-Wave Method. *Phys. Rev. B* **1994**, *50*, 17953.

(71) Kresse, G.; Furthmüller, J. Efficiency of *Ab-Initio* Total Energy Calculations for Metals and Semiconductors Using a Plane-Wave Basis Set. *Comput. Mater. Sci.* **1996**, *6*, 15−50.

(72) Perdew, J. P.; Chevary, J. A.; Vosko, S. H.; Jackson, K. A.; Pederson, M. R.; Singh, D. J.; Fiolhais, C. Atoms, Molecules, Solids, and Surfaces: Applications of the Generalized Gradient Approximation for Exchange and Correlation. *Phys. Rev. B* **1992**, *46*, 6671.

(73) Grimme, S.; Antony, J.; Ehrlich, S.; Krieg, H. A Consistent and Accurate *Ab Initio* Parametrization of Density Functional Dispersion Correction (DFT-D) for the 94 Elements H-Pu. *J. Chem. Phys.* **2010**, *132*, 154104.

(74) Henkelman, G.; Uberuaga, B. P.; Jónsson, H. A Climbing Image Nudged Elastic Band Method for Finding Saddle Points and Minimum Energy Paths. *J. Chem. Phys.* **2000**, *113*, 9901−9904.